Meter-scale MICP improvement of medium graded very gravelly sands: Lab measurement, transport modelling, mechanical and microstructural analysis

Guijie Sang [*], Rebecca J. Lunn, Grainne El Mountassir, James M. Minto

Department of Civil and Environmental Engineering, University of Strathclyde, Glasgow, UK

ARTICLE INFO

ABSTRACT

Microbially induced carbonate precipitation (MICP) is a promising biogrouting method for ground improvement. Most studies to date have focused on MICP treatment of uniform clean sands, with few studies having been conducted at large-scale on well-graded soils more representative of in situ deposits. This study presents a laboratory meter-scale MICP test on medium-graded very gravelly sands. The MICP treatment was conducted in a radial flow cell (diameter: ~1 m; thickness: ~0.15 m) with an injection well located at the centre and a constant hydraulic head at the outer boundary to replicate field conditions. Aqueous chemistry of the effluent samples inside the flow cell was continuously monitored. Transport modelling and effluent sampling monitoring of the electrical conductivity and pH show that, in general, there was good delivery and reaction of the bacteria and chemicals in the radial flow cell, with some preferential flow paths being present. The MICP-treated soil was subjected to a series of hydraulic and mechanical tests and microstructural analysis. Interestingly, the bio-cemented medium-graded very gravelly sands had higher strengths (UCS values of 2.6–7.4 MPa) for a given calcite content (9.2–15.1%) than those in comparable studies where uniform soils have been treated. This can be attributed to the higher initial density of grain-to-grain contact points in the medium-graded soil, and a high grain angularity which resulted in particle interlocking and longer grain-to-grain contact surfaces, as can be seen from Scanning Electron Microscopy images. Consolidated-drained triaxial tests on two cores showed peak deviatoric strengths of 5.9 MPa and 3.7 MPa under an effective confining stress of 100 kPa, with the clear formation of shear bands during shearing, compared to a peak deviatoric strength of 0.5 MPa determined for the untreated soil. MICP treatment clearly enhanced the shear strength and stiffness of the material. The study shows that formation of preferential flow paths may be a challenge for producing uniform biocementation in field applications of MICP. We propose that successful MICP treatment in heterogeneous soils will require a well-designed and well-executed site investigation programme that can identify, a priori, the geometry of any significant high or low permeability features within the soil body to inform the final MICP treatment strategy.

1. Introduction

Biomineralisation via ureolysis is a naturally occurring metabolic phenomenon that has been extensively studied in recent years as a promising grouting technique for ground improvement (Al Qabany and Soga, 2013; DeJong et al., 2006; Nafisi et al., 2020; Stocks-Fischer et al., 1999; Terzis and Laloui, 2018; Whiffin et al., 2007). This engineered process is commonly referred to as Microbially Induced Carbonate Precipitation (MICP). The most extensively investigated microorganism for MICP is *Sporoscarcina pasteurii* (*S. pasteurii*), a soil microbe that produces a highly active urease enzyme, which enables it to catalyse the

hydrolysis of urea and results in the production of ammonia and carbonic acid (Mobley et al., 1995). The highly soluble ammonia effectively increases the pH of the solution, which promotes carbonic acid to form bicarbonate and subsequently carbonate ions. If calcium sources are available, then the high pH promotes calcium carbonate precipitation with the negatively-charged bacterial cell surfaces acting as a nucleation site for calcium carbonate crystal formation. The formation and growth of calcium carbonate within the pore space of soils (Stocks-Fischer et al., 1999) has been shown to increase compressive, shear and tensile strength and stiffness (Al Qabany and Soga, 2013; DeJong et al., 2006; Terzis and Laloui, 2018; Whiffin et al., 2007; Zeng et al., 2021b). As a

---

* Corresponding author.
E-mail address: guijie.sang@strath.ac.uk (G. Sang).

result, MICP has been proposed for soil stabilisation (Al Qabany and Soga, 2013), for settlement reduction (Martinez and DeJong, 2009), to mitigate liquefaction (Montoya and Dejong, 2013), and to improve resistance to wind and water driven erosion (Cheng et al., 2021; Gomez et al., 2015; Liu et al., 2021; Salifu et al., 2016; Xiao et al., 2022). The MICP process is schematically described in Fig. 1.

Most of the studies to date investigating the influence of MICP on the geotechnical behaviour of soils have been conducted at small-scale, treating soil columns in the range of 10-100 mm in diameter and 20-250 mm in length (Al Qabany and Soga, 2013; DeJong et al., 2006; Nafisi et al., 2020; Tagliaferri et al., 2011). Few large-scale and field-scale MICP trials for soil improvement have been reported. As in small-scale studies the following large-scales studies all adopted a two-phase grouting approach, i.e. Phase 1. augmenting/stimulating bacteria (+/− fixer, +/− nutrients) and Phase 2. Circulation of cementing solution $CaCl_2$ & Urea, (+/− nutrients). (van Paassen et al., 2010) conducted a large-scale (100 m^3) MICP experiment and demonstrated that the stiffness and strength of the treated sands could be significantly improved, and that in situ geophysical (seismic) measurement is a feasible and effective tool to monitor the distribution of mechanical properties without disturbing the ground. The study set up a benchmark for a subsequent field trial with the aim of strengthening gravel layers under field conditions for borehole stability (van Paassen, 2011). This was the first pilot bio-grouting application on coarser soils (gravel) in the field. Although the presence of mineralised $CaCO_3$ was confirmed in the field trial, the evidence of good cementation over the treated area was not reported due to the limited resolution of seismic velocity and the difficulty in coring the gravel layers. (Gomez et al., 2015) performed in situ surficial application of MICP via surface percolation at a mine site located in Saskatchewan, Canada, with the aim of improving the erosion resistance of surface loose sand deposits for dust control and for potential re-vegetation. The treated depth of 28 cm (target depth 30 cm) was achieved using a strategy of applying a low-concentration cementing solution (urea and calcium chloride). This surface percolation treatment method, through which the infiltration rate is mainly driven by gravity and capillary forces, is highly dependent on soil properties which can act to limit the treatment depth and may cause clogging and non-uniform cementation (Cheng and Cord-Ruwisch, 2014). (Gomez et al., 2017a) performed a large-scale MICP trial on poorly-graded concrete sand (treatment thickness: 0.3 m; diameter: 1.7 m) using bio-augmentation and biostimulation of in situ bacteria, they found that

native ureolytic microorganisms may be stimulated to provide soil improvement. (Wu et al., 2020) conducted two MICP tests (one in pure silica sand, and the other in a sand/rock mixture) in a 1 m^3 container using a two-step grouting strategy, i.e. preliminary and secondary treatments, each involving five rounds of treatment. After ten rounds of treatment, the conversion of the total supplied calcium into precipitated calcium carbonate in the sand or sand/rock mixture was estimated to be above 90%. The achievement of this high conversion efficiency was attributed to recirculation of the cementing solution during the 1st five rounds of treatments, and to the surface percolation treatment for diverting flow to the target zone before the 2nd five rounds of treatments. Recently, a field trial was performed by (Zeng et al., 2021b) on fine-grained silty soils, with a much lower conversion efficiency of MICP. Modelling and fluid monitoring showed that only ~5% of the total soil volume was treated due to the heterogenous soil profile and the presence of a large number of fines, which resulted in preferential flow paths and even in hydraulically induced fractures. Xiao et al. (2022) conducted MICP trials on soils with different gradations for the prevention of slope erosion. They found that the efficacy of MICP treatment is highly influenced by soil gradation, and that the erosion of well-graded slope soils can be effectively mitigated using MICP, whilst the surficial erosion of poorly-graded soils can be intensified via MICP treatment. Most recently, (Sharma et al., 2022) conducted a large-scale (1.35 m × 1.13 m × 0.65 m) biocementation experiment on poorly graded Narmada river sand. The authors demonstrated an effective improvement in liquefaction resistance using co-cultivated hybrid bacteria (i.e. *Sporosarcina pasteurii* and *Bacillus sphaericus*).

Large-scale MICP trials provide crucial information regarding the feasibility, opportunities and challenges of applying biocementation processes at commercial scales. However, the majority of large-scale MICP trials to-date have focused on either uniformly graded or poorly graded soils (Gomez et al., 2015, 2017a; Sharma et al., 2022; van Paassen et al., 2010; van Paassen, 2011; Wu et al., 2020; Zeng et al., 2021a) (classification according to British Standard Institution BSI, EN ISO 14688-2:2018). A large-scale MICP trial on soils with a broad particle size distribution consisting of gravels, sands and fines is still lacking. Soil type, and heterogeneity, are key factors influencing MICP performance (Chae et al., 2021; Cheng et al., 2017; Ismail et al., 2002; Terzis and Laloui, 2018; Xiao et al., 2021), since they directly relate to the physicochemical attachment and physical straining of the microbes, and the flow and transport of the treatment solutions. In this study, we
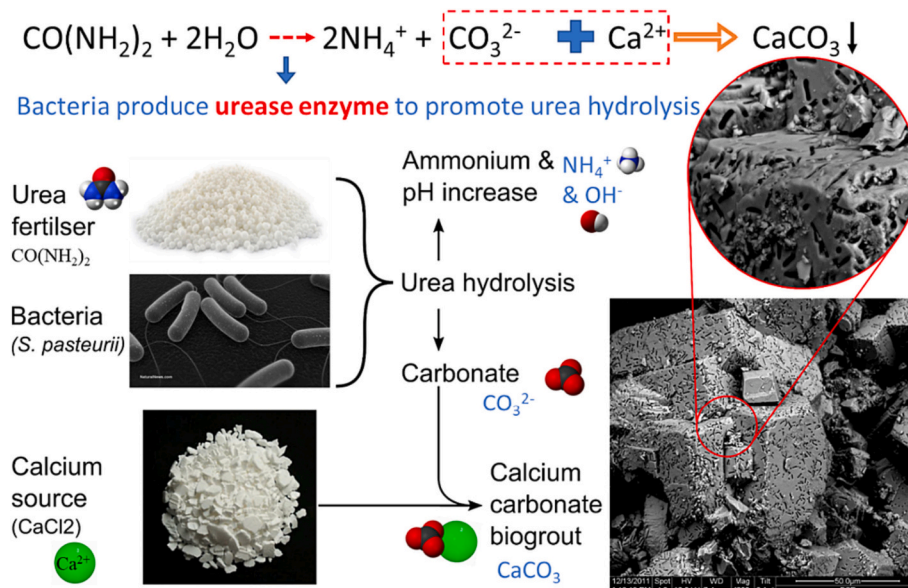

$$CO(NH_2)_2 + 2H_2O \dashrightarrow 2NH_4^+ + CO_3^{2-} + Ca^{2+} \Rightarrow CaCO_3 \downarrow$$

Bacteria produce **urease enzyme** to promote urea hydrolysis

Urea fertilser
$CO(NH_2)_2$

Bacteria
(S. pasteurii)

Calcium source
(CaCl2)
Ca^{2+}

Ammonium & pH increase
NH_4^+
& OH^-

Urea hydrolysis

Carbonate
CO_3^{2-}

Calcium carbonate biogrout
$CaCO_3$

Fig. 1. Schematic plot of the process of microbial induced calcite precipitation.

performed a meter-scale laboratory MICP test on medium-graded very gravelly sands consisting of 3.9% fines (< 63 μm), with a uniformity coefficient of 10.0 and a coefficient of curvature of 0.63 (classification according to British Standard Institution BSI, EN ISO 14688-2:2018). The test was performed in a constructed radial flow cell (dimeter: ~1 m; thickness: ~15 cm) with an injection well at the centre and a constant hydraulic head at the outer boundary to replicate the grouting conditions in the field. The post-treated soils were cored and a series of mechanical tests and microstructural analyses were performed including permeability tests, unconfined compressive strength tests, determination of calcium carbonate content, triaxial tests, SEM imaging and X-CT scanning. Transport modelling and effluent monitoring were also conducted for a better understanding of the biocementation process in the radial flow cell. The overall aim of this study is to assess the feasibility of the MICP strategy for improvement of medium-graded soils at large-scale, in order to guide future deployment of MICP in the field soils with increasingly complex composition.

2. Materials and experimental methods

2.1. Soil property and bacterial strain inoculation

185 kg of moist soil samples were used for the MICP test. The soil samples were collected from a local quarry in Kilsyth (Scotland, UK) with a natural water content of 7.6%. The particle size distribution (PSD) of the soils, as shown in the Supporting Information (SI) - Fig. S1, was determined by the British standard wet sieving method (BS 1377:1975, Test 7A) (Head, 1980). The soil consists of 31.4% gravels (2–10 mm), 64.7% sands (63 μm - 2 mm), and 3.9% fines (< 63 μm), indicating a very gravelly sand (BS5930). From the PSD curve, the median grain size (d_{50}) was determined as 0.75 mm. The grain sizes for which 60%, 30% and 10% of the grains by mass are finer were determined as 1.175 mm, 0.296 mm and 0.118 mm respectively giving a uniformity coefficient (d_{60}/d_{10}) and coefficient of curvature ($d_{30}^2/d_{60}/d_{10}$) of approximately 10.0 and 0.63, respectively, indicating a medium-graded very gravelly sands according to British Standard Institution BSI (EN ISO 14688-2:2018) (BSI, 2018). The soils were moist-packed into the radial flow cell (diameter: 1 m, thickness: 0.135 m) with a porosity of 27.6% and a pore volume of 26 L.

The ureolytically active bacterial strain *S. pasteurii* (DSM No. 33) was taken from freeze dried stock (stored in −80 °C refrigerator) and initially used to inoculate 2 L of autoclaved yeast extract media (5.5 g/L yeast extract, 5 g/L sodium chloride, 0.4 g/L D-glucose and 0.4 g/L potassium phosphate dibasic) supplemented with 20 g/L urea, contained in a 5 L flask. The inoculated media was then incubated at a temperature of 30 °C on an orbital shaker at 115 rpm for ~24 h. After 24-h cultivation, the bacterial optical density at a single wavelength of 600 nm (OD_{600}) was ~1.3, as determined by a UV-VIS spectrophotometer. The 2 L of bacteria grown in the yeast-extract media was then used to inoculate aerobically (aeration rate: 9.2 L/min) a 50 L fermentation tank filled with 40 L of yeast extract media at 30 °C. Growth in the 50 L fermentation was allowed to take place over approximately 24 h. Around 42 L of media with an OD_{600} of ~1.6 was then harvested and stored in the cold room (4 °C) for further use. As the MICP cycles proceeded, 3 L of the stored bacterial solution was used to inoculate fresh media in the 50 L fermentation tank (24 h, 30 °C, 9.2 L/min aeration rate) for the supply of bacteria for used in each treatment cycle. The bacteria in the media were harvested and diluted with tap water to ~1 OD_{600} for injection. The specific urease activity of the bacteria was determined using the conductivity method (Whiffin, 2004). Specifically, 2 ml of ~1.0 OD_{600} bacteria solution was added into 18 ml 1.11 M urea, with the electrical conductivity (E. C.) measured over a period of 10 min. The rate of change in E. C. (μS/cm/min) was converted to the rate of change in urea concentration (mM/min) using a conversion factor of 10.62 (Minto et al., 2016).

2.2. Radial flow cell construction and MICP treatment strategy

A schematic plot of the radial flow cell is shown in Fig. 2.The radial flow cells consists of a central injection well (outer diameter: 2 cm), a top cover (to provide confinement) and a base (each 20 mm thick clear acrylic), and a perforated plastic sheet around the outer boundary. The injection well contains evenly-distributed perforated holes (diameter: 2.5 mm; spacing: 2.3 mm) screened by a 120 M polyester silk mesh to avoid back flushing of fine particles. The overall diameter and thickness of the radial flow cell are 0.94 m and 0.15 m, respectively. 185 kg of the very gravelly sand was moist packed into the radial flow cell, with its thickness being 0.135 m after being fully saturated with tap water. Between the soil layer and the top cover, a layer of kaolin (0.015 m) was emplaced. Due to its low permeability and high ductility kaolin was emplaced to avoid bypass flow along the top cover of the flow cell. Between the soil layer and the kaolin layer a deformable and impermeable cling film layer was placed to avoid migration of kaolin particles during treatment. The radial flow cell was submerged under tap water within a larger surrounding tank, with a constant water level maintained (~10 cm above the top of the kaolin layer) to replicate a constant fully saturated pressure condition at the outer boundaries. In addition, three 25 L containers filled with tap water were placed on top of the top acrylic sheet in order to increase the confining stress applied to avoid bypass flow. In order to collect effluent samples, a 3.2 mm diameter plastic tube was buried in the radial flow cell during the soil packing process, with the tube head located at a distance of 25 cm to the northwest boundary. The tube head was screened with a 120 M mesh to avoid the migration of particles into the tube. A peristaltic pump provided a small suction pressure for effluent sampling at a rate of 5 ml/min, which was small enough to not to disturb the pressure distribution of the radial flow cell, but still large enough to sample the fluids in the case that clogging occurred near the sampling port due to calcium carbonate precipitation.

Prior to MICP treatment, 28 L of sodium chloride solution (20 mM) was injected as a tracer into the radial flow cell at a flow rate of 1.35 L/min, followed by an injection of 28 L of tap water (same flow rate) to displace the saline solution. Effluent samples at a location of 25 cm from the northwest boundary were collected every two minutes (sampling rate: 5 ml/min) using the peristaltic pump. The electrical conductivities of the effluent samples were subsequently measured. This procedure was conducted to confirm a relatively radial flow pattern without significant bypass flow, prior to MICP treatment.

In total 9 cycles of MICP treatment were carried out. For each cycle, two pore volumes of bacteria solution (volume: 52 L, ~1 OD_{600}) were injected using an air compressor pump at an initial rate of 2.88 L/min. Immediately after the injection of the bacterial solution, 260 ml tap water (influential diameter ~ 5 cm) was injected for well cleaning to avoid clogging near the injection well, followed by an hour static period (i.e. no flow) to allow bacterial settlement and attachment. Then one pore volume (26 L) of cementing solution (0.5 M urea & 0.5 M CaCl₂) was injected using a screw pump (with lower pulsation) at an initial flow rate of 1.6 L/min. After a 4-h reaction period, a second pore volume (26 L) of cementing solution (0.5 M urea & 0.5 M CaCl₂) was injected at the same flow rate. The flow cell was then left static overnight until the next treatment cycle. Each treatment cycle lasted for one day, with the exception of cycles 3 and 4, which were left static for two days due to laboratory access constraints. Note that due to the decreased permeability during later cycles, the injection flow rates of the bacteria and cementing solutions were reduced accordingly to avoid severe pressure build-up at the injection point. The effluent samples were collected continuously during the injection process and then collected periodically during the static/reaction period. pH and EC of the effluent samples were measured after effluent collection.

The pressures at the injection well (p_0) and at the sampling port (p_1) were monitored during the injection of cementing solution. The outlet pressure (p_2) at the boundary was maintained constant (i.e., the
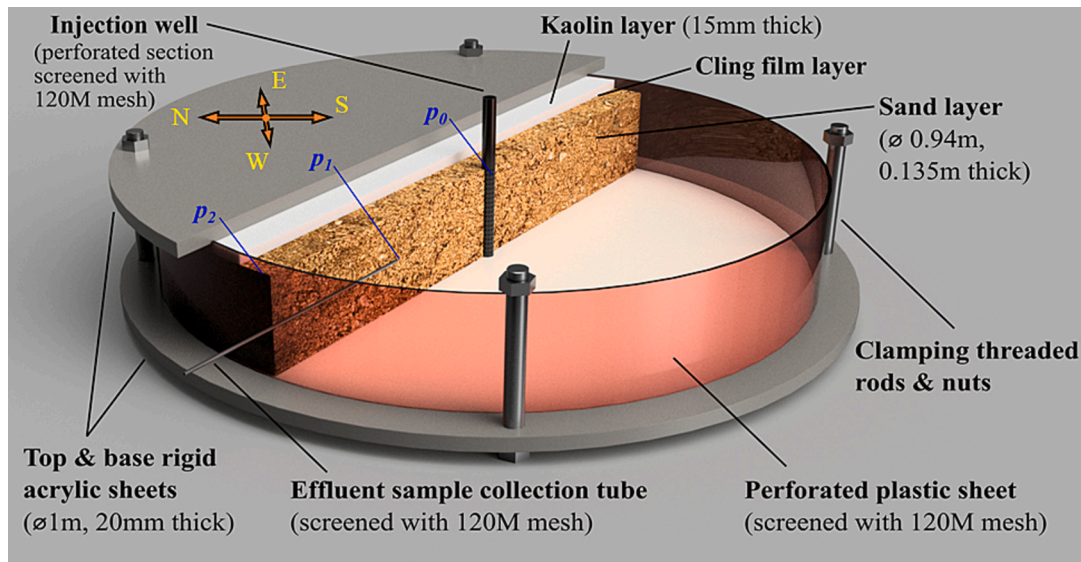
Fig. 2. Schematic plot of the radial flow cell.

hydraulic head was 10 cm above the soil layer). Permeability k [L^2] of the soil in the radial flow cell was calculated based on Darcy's law for radial flow, as shown in SI Fig. S2 in the supporting information, and given by

$$k = \frac{q\mu}{2\pi h} \bullet \frac{ln(r_i/r_j)}{p_i - p_j} \tag{1}$$

where q [L^3/T] is the injection rate; h [L] is the thickness of the radial flow cell; μ [M/L/T] is the dynamic viscosity; p_i and p_j ($i, j = 0, 1, 2; i \neq j$) are the pressures at the radius of r_i and r_j respectively.

2.3. Tracer/bacteria breakthrough in 1-D columns

To better understand the transport of the chemicals and the retention of bacteria in the radial flow cell, tracer/bacteria breakthrough tests were conducted in three 1-D columns (diameter: 28 mm; length: 280 mm) packed with the same very gravelly sand (under saturated conditions) at three different Darcy velocities, i.e., 50 cm/h, 100 cm/h and 200 cm/h, respectively. Note that the sands in the 1-D columns were homogeneously mixed and packed such that the porosity (27.6%) and permeability (1.6 × 10^{-12} m^2) match those in the RFC (porosity = 27.6%, permeability = 1.9 × 10^{-12} m^2). The three velocities were equivalent to those in the radial flow cell at distances to the central injection well of 0.4 m, 0.2 m, and 0.1 m, respectively. Specifically, 2 pore volumes of bacteria solution, which were from the same batch as used for the 9th MICP treatment cycle, were injected into the three columns at the selected velocities. After an hour static time, 2 pore volumes of 1.5 M NaCl solution were injected at the same velocity to replicate the ionic strength of the cementing solution, i.e., 0.5 M CaCl$_2$ and urea solution. Note that these column breakthrough tests were conducted to provide a better understanding of the transport of the chemicals and the bacteria in the saturated soils. The replacement of cementing solution (0.5 M CaCl$_2$ and urea) with 1.5 M NaCl at the 2nd stage of the column breakthrough test was to exclude any effects of bio-chemical reactions (i.e. biomineralisation). For the cases of the column tests under a Darcy velocity of 50 cm/h and 100 cm/h, 5 pore volumes of tap water (ionic strength equivalent to ~0.5 mM NaCl) were injected in a 3rd stage to check whether bacteria were released under the elution of tap water. This process was to validate whether the injection of a small amount of tap water could be successfully used for well cleaning to avoid clogging near the injection zone in the radial flow cell.

2.4. Testing the MICP-treated samples in the radial flow cell

2.4.1. Coring

After the completion of 9 cycles of MICP treatment, the treated soil in the radial flow cell was cleaned by flushing ~4 PV of tap water to remove any residual chemicals and bacteria. The top cover of the radial flow cell and the upper layer of kaolin were removed. A quick acoustic assessment was conducted, by tapping the top of the treated soil using the back of a steel spoon, to roughly evaluate the spatial variations in stiffness of the treated soil. Subsequently, 35 mm diameter cores were drilled from the post-MICP-treated sands for hydromechanical tests as shown in Fig. 3. Fig. 4 shows the schematic of the sampling locations for the permeability and strength tests. Note that the medium-graded very gravelly sand has a very broad size distribution and consists of 31.4% gravels (>2 mm), hence, it was extremely challenging to drill long intact cores due to the large angular grains present. When the coring bit cut the gravel particles or the bigger sand particles, the core machine started to shake dramatically. The disturbance of the coring bit, in turn, induced a local stress concentration at the cutting point and broke several of the samples, an issue that (van Paassen, 2011) also encountered when drilling cores from gravel layers in their field trial. Apart from the stress perturbance (especially for gravelly sands) induced by the coring bit, the coring process also tends to cause a relaxation of the stress and strain, thus weakening the cementation bonds if the released stress exceeds the cohesive forces of the bio-cemented sands. This might cause an underestimate of the overall strength tested under unconfined or triaxial compression conditions.

2.4.2. Permeability test

The drilled cores were first of all subjected to permeability testing using a core holder under different confining stresses, i.e. 50 kPa, 100 kPa, 200 kPa, 300 kPa, 400 kPa and 500 kPa. It was found that permeability dropped sharply at confining stresses from 50 kPa to 200 kPa, but was maintained almost unchanged at confining stresses larger than 200 kPa (see SI Fig. S3). We attribute this to the "wall effect", i.e. the presence of bypass flow between the rubber jacket and surfaces (angular gravel grains) inside the core holder, occurring at confining stresses below 200 kPa. Further increasing the confining stress (>200 kPa) induced a slight pore shrinkage and thus induced a slight permeability reduction (SI Fig. S3). Therefore, 200 kPa was selected as the confining stress for determining permeability.
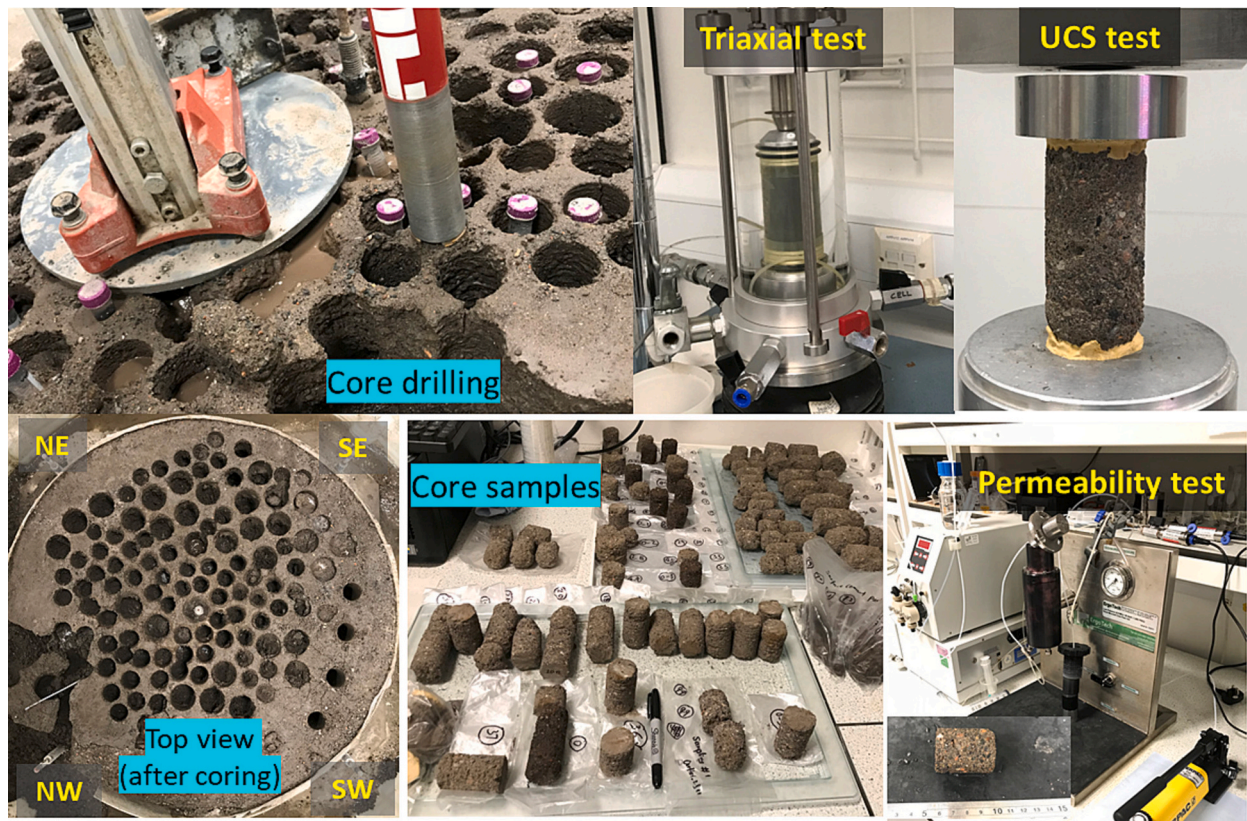
Fig. 3. Core sampling of the post MICP treated soils and hydro-mechanical tests, i.e. permeability test, UCS test, and triaxial test of the core samples.

2.4.3. Unconfined compressive strength

After performing the permeability test, core samples were oven-dried and then subjected to an unconfined compressive strength (UCS) test. Prior to the UCS test, the top and bottom surfaces of the core samples were capped with gypsum plaster (Crystacast, compressive strength of 55.2 MPa) to ensure surface flatness to avoid the occurrence of stress concentrations during loading. A loading rate of 0.5 mm/min was applied until failure. After the UCS test, the $CaCO_3$ content of each core sample was determined using a carbonate analyser based on the standard test method for rapid determination of carbonate content of soils (ASTM-D4373). The carbonate analyser, which was calibrated using pure $CaCO_3$ powders, consisted of a reaction cylinder, a smaller container inside the cylinder for the isolation of acid from soil samples, and a pressure gauge. For each UCS tested core sample, ~4–6 g of the sample were oven-dried and pulverized into fine particles (<0.425 mm). The calcite content was then determined according to ASTM-D4373. $CaCO_3$ content is reported as the mass of calcite/mass of dry sands.

2.4.4. Triaxial compression testing

An untreated sample and two core samples, one drilled near the injection well (sample_#1) and the other drilled near the sampling port (sample_#2) as marked in Fig. 4, were subjected to consolidated drained triaxial testing at an effective confining stress of 100 kPa. The two treated samples were first immersed in de-aired water under vacuum conditions for 1–2 days until no more bubbles were observed. The untreated sand was partially moist with de-aired water and then packed in a triaxial mould. Once the samples (treated and untreated) were mounted in the triaxial cell, they were subjected to a further de-airing process by flushing de-aired water into the sample until no bubbles were observed in the effluent. This was followed by applying a simultaneous linear increase to the cell and back pressures up to 600 kPa and 550 kPa, respectively, so as to force any residual air to dissolve into the pore water. Subsequently, the B-check process, i.e., a short test of

Skempton's B-value (Skempton, 1954), was performed by applying an incremental cell pressure increase of 50 kPa whilst the specimen drainage port remained closed. During the B-check stage, the B values for the two cores and the untreated sample were 95.0%, 95.6%, and 95.1% respectively, indicating sufficient saturation. After the B-check, the specimens were consolidated to achieve the target stress condition, i. e., a cell pressure of 700 kPa and a back pressure of 600 kPa, resulting in an effective confining stress of 100 kPa. Finally, the specimens were sheared (under a drained state) by applying an axial strain rate of 0.05 mm/min.

2.4.5. SEM imaging and X-CT scanning

The microstructures of the biocemented very gravelly sand specimens were analysed based on Scanning Electron Microscopy (SEM) in the Advanced Materials Research Laboratory (ARML), at the University of Strathclyde, Glasgow. The specimens were sputter-coated with gold. Backscattered SEM images were collected at an accelerating voltage of 15 kV on one polished block prepared by an external specialized sample preparation laboratory. The polished block was prepared by impregnating the specimen with resin, in order to obtain an optimum polishing quality. For the core sample with the highest unconfined compressive strength, secondary electron images were collected on a bean-sized specimen (length: ~1 cm) collected near to the failure plane without being polished. Meanwhile, energy dispersive spectroscopy (EDS) was also conducted for the quantitative analysis of the chemical composition to distinguish precipitated $CaCO_3$ crystals from sand, gravel and silt grains.

A core sample near the sampling port was scanned with a Nikon XT H 225 LC X-ray computed tomography system fitted with an 225 kV X-ray source at the ARML, University of Strathclyde, Glasgow. The 3D volume reconstruction was performed using Nikon XTekCT software version 4.3.4. The scanning parameters were 120 kV, 150 μA, 1000 m-second exposure, and 3141 projections, with a voxel size of 22 μm.
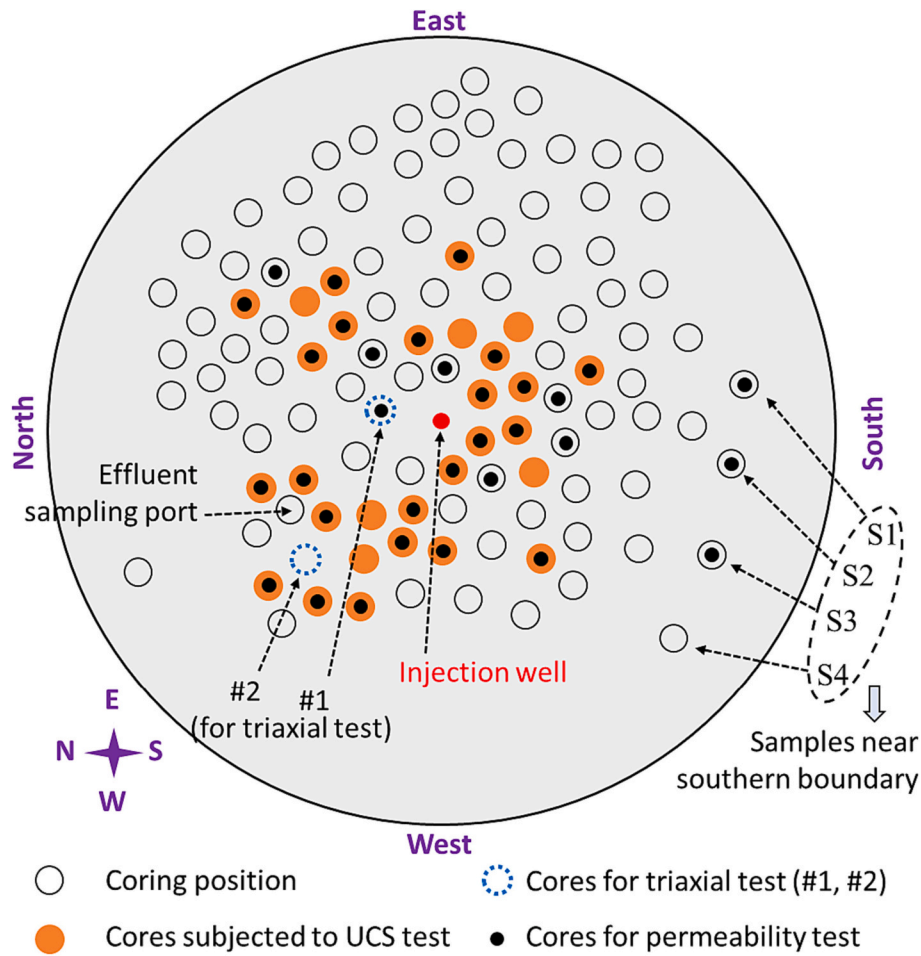
Fig. 4. Schematic plot of core location and direction, with cores marked by black circle, cores for UCS and permeability tests are marked by orange and black dots, respectively. Two cores for triaxial tests are labelled by #1 and #2, four samples near the southern boundary are labelled S1-S4.

3. Transport modelling of the bacteria and the tracer test

The following advection-dispersion equation was applied to model the transport of both the bacteria and the tracer in the soil under a saturated state (Sang et al., 2023; Tan et al., 1994):

$$\frac{\partial(\phi C)}{\partial t} + \frac{\partial(\rho_{\mathrm{b}} S)}{\partial t} = \nabla \bullet \phi D \nabla C - u \bullet \nabla C \tag{2}$$

$$\frac{\partial(\phi c)}{\partial t} = \nabla \bullet \phi D \nabla c - u \bullet \nabla c \tag{3}$$

where t is time [T]; ϕ [−] is the porosity of the soil; C [N_c/L^3] is the concentration of bacteria suspended in the aqueous solution (i.e., the number of cells per unit volume of the solution) and c [M/L^3] is the concentration of the tracer; ρ_{b} [M/L^3] is the bulk density of the dry soil; S [N_c/M] is the number of bacterial cells per unit mass of solid particles. Accordingly, ($\rho_{\mathrm{b}} \cdot S/\phi$) is the deposited bacterial concentration analogy to aqueous bacterial concentration C, defined as the number of bacterial cells attached on the solid particles per unit volume of pore-solution. u [L/T] is the Darcy velocity; D [L^2/T] is the dispersion coefficient, which is a function of the hydrodynamic dispersivity α_d [L], and effective diffusion coefficient d_c [L^2/T] as: $D = \alpha_d u/\phi + d_c$ (Minto et al., 2019; Tobler et al., 2014); S [N_c/M] is the concentration of bacteria deposited on the solid particles (number of cells per unit mass of solid particles), which can be expressed as (Sang et al., 2023)

$$\frac{\rho_{\mathrm{b}}}{\phi}\frac{\partial(S)}{\partial t} = K_c \psi C - \frac{\rho_{\mathrm{b}}}{\phi} K_{\mathrm{d}} S \tag{4}$$

$$\psi = e^{-S/\lambda} \tag{5}$$

where K_c [1/T] is the first-order deposition rate, including both physicochemical attachment and pore straining; K_{d} [1/T] is the first-order detachment rate; ψ is a dimensionless decay function; λ is a decay constant, with dimensions the same as S [N_c/M]; ψ quantifies the exponential decline of deposition rates due to the effect of site blockage (Sang et al., 2023; Xu et al., 2006).

The above equations were solved by a finite-element-based COMSOL Multiphysics. Specifically, the effluent breakthrough of bacteria and tracer (NaCl solution) in the columns were simulated using a 1-D domain consisting of 280 subdomains (i.e. each element size was 1 mm). Details of the modelling simulation of the 1-D transport of tracer and bacteria can be found in (Sang et al., 2023). The effluent breakthrough of the tracer (NaCl solution) in the radial cell was simulated using a 2-D domain as shown in SI Fig. S4 (1/4 geometry was simulated due to the symmetry in geometry and the isotropy of the hydraulic and transport properties), with the domain being discretised into 21,493 triangular elements. Transport of the tracer in the radial cell was modelled using the same equation (i.e. Eq. (3)) as that used in the 1-D columns, with the same hydrodynamic dispersivity α_d and effective diffusion coefficient d_c as those used in the 1-D columns. In addition, the flow in the radial cell was solved by Darcy's law, given by

$$v = -\frac{k}{\mu}\nabla p \tag{6}$$

where v is the Darcy velocity [L/T]; ∇p is the pressure difference [M/L^2/

T^2]; μ is the dynamic viscosity [M/L/T]; k is the permeability [L^2]. The numerically simulated flow velocity along the radial length is an excellent match to the analytical solution, based on Eq. (1), as shown in SI Fig. S5. Note that in upscaling the simulation of tracer transport from 1-D columns to the 2-D radial flow cell in this study, it is assumed that the saturated sands in the column are homogeneously mixed and that they have the same hydraulic properties, i.e. that there are no preferential flow paths in either the 1-D or 2-D simulations.

4. Results

4.1. Ureolytic activity of the bacteria

The change in EC during the 10-min urease activity test is shown in SI Fig. S6. The specific urease activity of the bacteria for each treatment cycle was calculated based on the conductivity method. The specific urease activity for the 9 cycles of MICP treatment ranged from 1.79 to 2.96 mM/OD_{600}/min, with an average urease activity of 2.43 mM/OD_{600}/min (SI Fig. S7). The EC and pH values of the injected bacterial solution are shown in SI Fig. S8 (*a*), with the average EC and pH being 24.8 mS/cm and 9.5 respectively. The EC and pH values of the cementing solution (consisting of 0.5 M urea & 0.5 M $CaCl_2$) are given in SI Fig. S8 (*b*), with the average EC and pH being 83.4 mS/cm and 10.2 respectively.

4.2. Tracer and bacteria transport in the soils

4.2.1. Transport in the 1-D columns

Modelled and measured breakthrough curves of the tracer (NaCl) and the bacteria in the three columns (diameter: 28 mm; length: 280 mm) under Darcy velocities of 200 cm/h, 100 cm/h, 50 cm/h, are shown in Fig. 5 (*a*) and (*b*), respectively. Model fitting of the tracer (NaCl) breakthrough curves (Fig. 5*a*) gives a hydrodynamic dispersivity (α) and an effective diffusion coefficient (d_c) of 1.0×10^{-2} m and 1×10^{-9} m^2/s, respectively. The modelling parameters for bacteria deposition are given in SI Table S1. Overall, model results agree well with the measured results. Fig. 5 (*b*) shows the modelled and observed bacteria breakthrough curves in the 1-D columns under the three tested velocities. The normalized OD_{600} after the injection of 2 PV of bacteria solution is around 0.8 (less than the original bacterial OD_{600}), indicating bacteria retention in the soil. Initially, during the injection of 1.5 M NaCl solution, the measured bacteria breakthrough is slightly lower than the model results due to the 1-h static period, which allows bacteria to settle on the grain surfaces and pore constrictions and causes fewer bacteria to breakthrough. Note that the modelling parameters for all three tested velocities are the same. The slight difference in bacteria breakthrough

times (Fig. 5*b*) is due to the difference in residence times of bacteria in the columns. The effect of the velocity itself, i.e. the increasing hydrodynamic forces, on bacteria transport and on the deposition behaviour in the studied soils is negligible within the range of velocities tested.

4.2.2. Modelling transport in the radial flow cell

Prior to MICP treatment of the large radial flow cell, tracer (20 mM NaCl) breakthrough was monitored (Fig. 6*a*). This was to ensure there was no bypass flow in the radial flow cell prior to MICP treatment, so as to achieve an effective delivery of bacteria and cementing solutions in the radial flow cell. Similarly, changes in EC during the 1st, 3rd, 5th, and 7th cycle of the injections of bacteria solution and cementing solution were also monitored (Fig. 6*b*). Using the same model parameters, and assuming a negligible gravity effect, the EC of the effluent samples was simulated both before (Fig. 6*a*) and during (Fig. 6*b*), the 1st, 3rd, 5th and 7th cycles of the MICP treatment. Results show quite good agreement with the experimental test. However, it can be seen in Fig. 6 (*a*) and (*b*) that the experimental observations of the tracer breakthrough occur later than the model predictions. This likely occurs due to the formation of preferential flow paths in the other regions of the radial flow cell, resulting in a slight delay to tracer arrival at the sampling port. Note that during the injection of the 1st PV of cementing solution, the bacteria solution was gradually displaced by 0.5 M $CaCl_2$ solution near to the sampling port, resulting in an effluent sample consisting of both bacteria solution (with residual CO_3^{2-}) and cementing solution (with Ca^{2+}). This caused calcium carbonate to precipitate, resulting in a lower EC measurement (Fig. 6*b*).

4.2.3. Aqueous chemistry of the effluent samples

Fig. 7 (*a*) and (*c*) show the changes in EC and pH value at the sampling port in the radial flow cell monitored throughout the entire set of MICP treatment cycles. The initial EC and pH of the bacteria solution and cementing solution for each treatment cycle are shown in SI Fig. S8. From Fig. 7 (*a*), the evolution of EC shows a similar trend in each MICP cycle. Take the 3rd cycle for instance (detailed in Fig. 7*b*), the EC decreases with the injection of the bacterial solution, as shown in Fig. 7 (*b*) stage 1. This occurs as the injected bacteria solution had a lower EC than the residual cementing solution from the 2nd cycle. In stage 3, Fig. 7 (*b*), as the residual bacterial solution is displaced by the 1st PV of cementing solution, the EC starts to raise again. After the injection of the 2nd PV of cementing solution (stage 5, Fig. 7*b*) and during the overnight reaction period (stage 6, Fig. 7*b*), the EC near the sampling port slightly decreases, for a short period, and then continuously increases overnight. These observations are consistent with batch experiments, reported in SI Fig. S9 (*a*). Initially, the calcium cations consume the residual CO_3^{2-} and/or ureolytically produced CO_3^{2-} by a fast precipitation of calcium
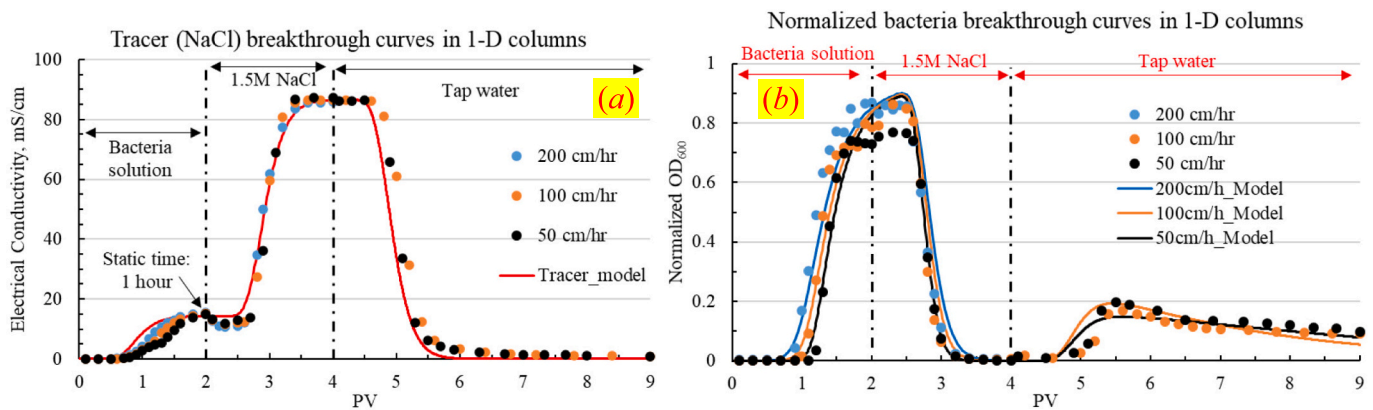

Fig. 5. Tracer (*a*) and bacteria (*b*) breakthrough curves in 1-D columns under different velocities (i.e. 200 cm/h, 100 cm/h, 50 cm/h). Effluent samples under the velocity of 200 cm/h during the 3rd stage (i.e. tap water injection) were not collected. The EC and pH values of tap water were 51.4 μS/cm and 7.7 respectively.
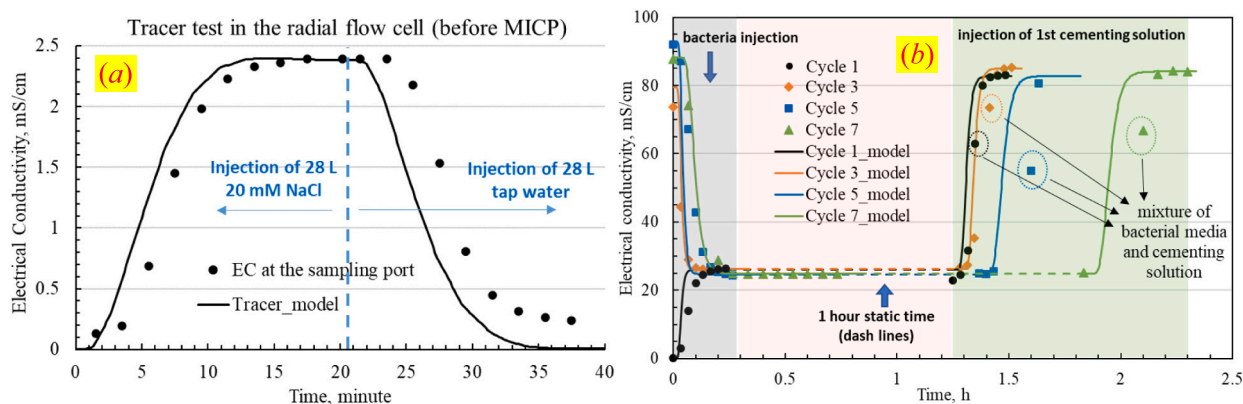
Fig. 6. (*a*) Tracer test in the radial flow cell prior to the MICP treatment cycles; (*b*) Changes in EC at the sampling port during the 1st, 3rd, 5th, and 7th cycle of injections of bacteria solution and cementing solution. The EC shifts to the right due to a reduction in the injection rates from the 1st to 7th injection cycles.
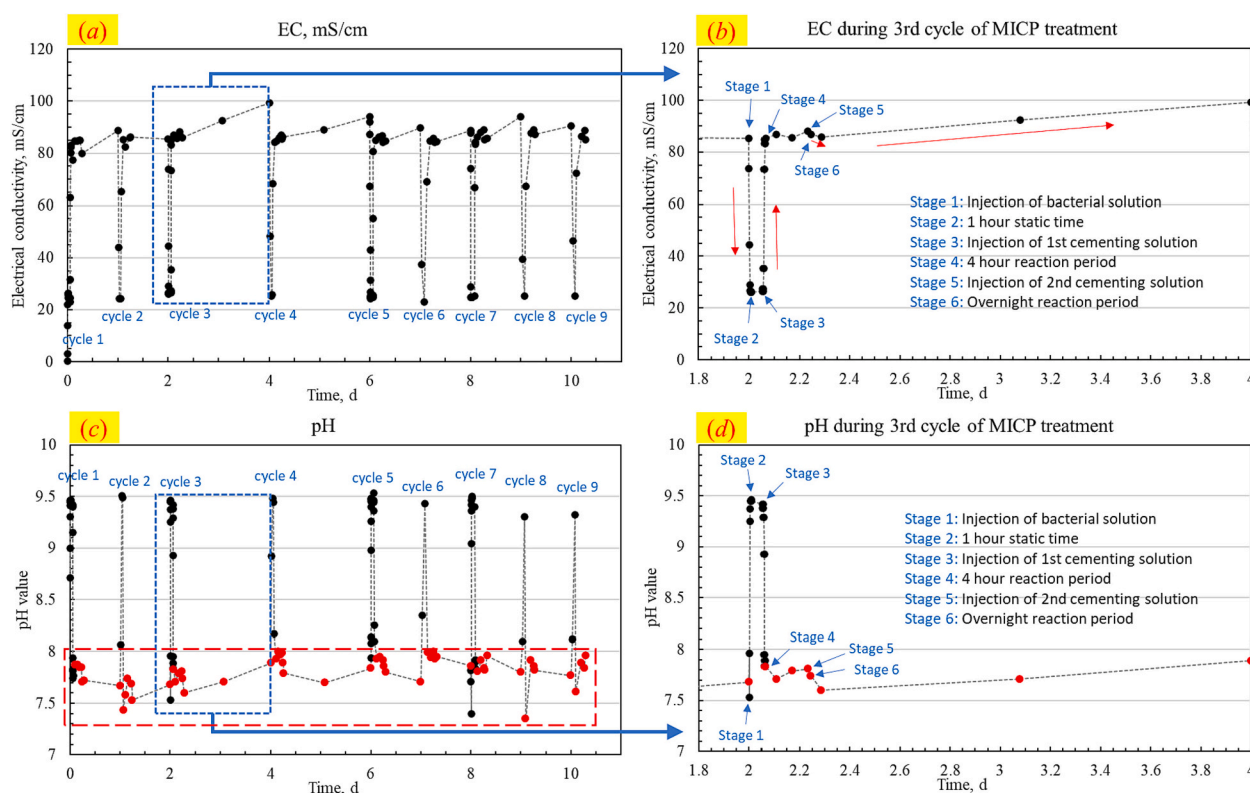

Fig. 7. Changes in (*a*) EC and (*c*) pH of the aqueous solution collected from the effluent port in the radial flow cell; zoomed values of (*b*) EC and (*d*) pH during the 3rd MICP treatment cycle.

carbonate (CaCO₃), inducing the slight decrease in EC; urea hydrolysis continues to decompose urea into ammonium and carbonate cations; while calcium carbonate is precipitated, ammonium chloride remains in solution contributing to the overall increase in EC. The continued increase in EC during the overnight reaction period indicates that urea hydrolysis continues to occur.

Injection of bacterial solution (pH ~ 9.5) increases the pH in the radial flow cell to 9.3–9.5 at the beginning of each treatment cycle as shown in Fig. 7 (*c*). After injection of the 1st PV of cementing solution, the pH at the sampling port ranges between 7.4 and 8.0 during all treatment cycles, as marked by solid red dots in Fig. 7 (*c*). This is lower than the pH of both the initial bacterial solution (pH ~9.5) (SI Fig. S8*a*) and the cementing solution (pH ~10.2) (SI Fig. S8*b*). This is consistent with the batch experiment reported in SI Fig. S9 (*b*), the presence of

calcium cations in the cementing solution consumes the microbially induced carbonate ions through calcium carbonate precipitation and simultaneously lower the pH values. Meanwhile, urea hydrolysis produces ammonia which tends to increase the pH value. The two effects counteract and limit changes in the solution pH to between 7.4 and 8.0. Unlike the batch experiment shown in SI Fig. S9 (*b*), the pH at the sampling port in the radial flow cell shows an initial decreasing, and subsequently increasing, trend in the 2nd, 3rd, and 4th cycles during the overnight reaction period (Fig. 7*c*). This may be caused by the existence of fluid containing residual carbonate ions (CO₃²⁻) originally from the injected bacteria media not being fully displaced during injection of the cementing solution. Once calcium cations (Ca²⁺) are consumed completely through calcium carbonate precipitation, further urea hydrolysis gradually increases the pH of the surrounding solution during

the 2nd, 3rd, and 4th cycles.

4.3. Permeability evolution

Fig. 8 shows the overall permeability of the soils in the radial flow cell, as measured during the injection of the cementing solution at each treatment cycle (the two permeabilities measured from the 1st and 2nd injection of cementing solution were very similar). The estimation of the permeability assumed a radial flow pattern according to Eq. (1) based on the three different pressure values monitored at the injection well (p_0), the sampling port (p_1) and the outer boundary (p_2), as schematically plotted in SI Fig. S2. The initial bulk permeability of the cell based on the monitored well pressure (p_0) and the outlet pressure (p_2) was estimated to be 1.9×10^{-12} m^2, which is very similar to the permeability of the pre-treated soils (1.6×10^{-12} m^2) measured in the 1-D column using the same packing density and porosity. As the MICP cycles proceeded, the overall permeability based on the injection well pressure (p_0) and the outlet pressure (p_2) remained almost unchanged during the first three cycles and then decreased abruptly during the 4th cycle. Subsequent to cycle 4, the permeability remained virtually unchanged until the 8th treatment cycle, after which it showed a slight decrease. Over the full experiment, the permeability decreased by approximately one order of magnitude which can be attributed to the precipitation of calcium carbonate. The initial permeability estimated from the difference in the injection pressure (p_0) and the pressure at the sampling port (p_1) is similar to that of the bulk cell permeability calculated using p_0 and p_2. However, the permeability estimated from the pressure (p_1) at the sampling port and the outlet pressure (p_2) is an order of magnitude higher than the bulk permeability estimated. This indicates that the soil between the effluent port and the northwest boundary was initially more permeable than the average value for the radial cell. As MICP cycles proceeded, the permeability of the northwest sector of the radial cell (i. e. between p_1 and p_2 as shown in SI Fig. S2) gradually decreased from 8.4×10^{-12} m^2 to 3.1×10^{-12} m^2 due to the precipitation of calcium carbonate, but remained for each cycle at a value higher than that of the average permeability for the radial flow cell. Based on these observations of permeability surrounding the sampling port, it is likely that other regions of the cell also vary significantly in permeability and that the radial flow pattern was not uniform during treatment.

The permeability of the core specimens, cored from the MICP-treated soil, were measured and plotted against the distance to the central injection well as shown in Fig. 9a. As expected, the permeability for each individual core is lower than that of the original soil (1.6×10^{-12} m^2) due to calcium carbonate precipitation. The permeability of the well-cemented specimens, as plotted by the blue solid dots in Fig. 9a,

ranged from 4.8×10^{-14} m^2 to 1.0×10^{-12} m^2, whilst the permeability of the poorly-cemented specimens near the southern boundary (red solid triangles in Fig. 9a) was lower, with one as low as 3.2×10^{-15} m^2. Fig. 9a also shows that MICP treatment cycles result in permeability decreasing with radial distance from the injection well. This may be caused by higher velocity and higher flux near the injection well. As shown in SI Fig. S5, the fluid velocity in the radial flow cell decreases sharply from the injection well to the outer boundary. Higher velocities near the injection well corresponded to higher hydrodynamic shear forces and hence could result in less bacterial deposition at grain surfaces, resulting in less calcite precipitation near the injection well and hence higher permeability. However, bacteria column breakthrough tests (Fig. 5b) and modelling analysis suggest that the effect of hydrodynamic forces on bacteria deposition for the soil conditions and velocities tested here (i.e. 50, 100, and 200 cm/h) is negligible (SI Table S1 also indiated that deposition parameters were independent of the tested velocities). In which case, since the fluid velocity should not affect the bacterial deposition, and a greater flux of both bacteria and cementing solution are experienced in this region, more calcium carbonate cementation would be expected. Clearly this disagrees with the negative correlation observed between the local permeability of the core samples and their distance from the injection well, as shown in Fig. 9a. The other possible explanation for the higher permeability observed near the injection well is the migration of fines in the soil. The initial injection of the bacteria solution (average rate: 2.88 L/min) could be sufficient to induce the migration of fine particles toward the outer boundary, leaving fewer fines near the injection well and hence higher permeability. This theory is well supported by the fact that the three soil samples (S1, S2, S3 labelled in Figs. 4 and 9b) cored near the southern boundary contained more fine particles than the original soil (SI Fig. S10). As a result, despite the lack of calcium carbonate precipitation, these three samples (S1, S2, S3) had a lower permeability than the cemented cores (Fig. 9a & b). Note that the precipitated CaCO$_3$ (total amount 1.7–2.1%) may contribute to the percentage of fines. However, this part may be minor since among the different CaCO$_3$ precipitation types (i.e. bridging between grains, coating on surfaces, filling in voids), only pore-filling could be flushed through and behave as fines. SI Fig. S11 also shows that for soil sample S4 (labelled in Fig. 4), collected near the southwest boundary, fine migration occurred and induced clogging in a 28 mm column at a Darcy velocity of 50 cm/h, which is equivalent to the velocity at a distance of 0.4 m from the injection well in the radial flow cell. The clogging of the column was likely induced by the migration of the accumulated fines (6.3%, as shown in SI Fig. S10) in this region. The migrations of fines could possibly result in a lower permeability near the southern boundary, producing preferential flow paths
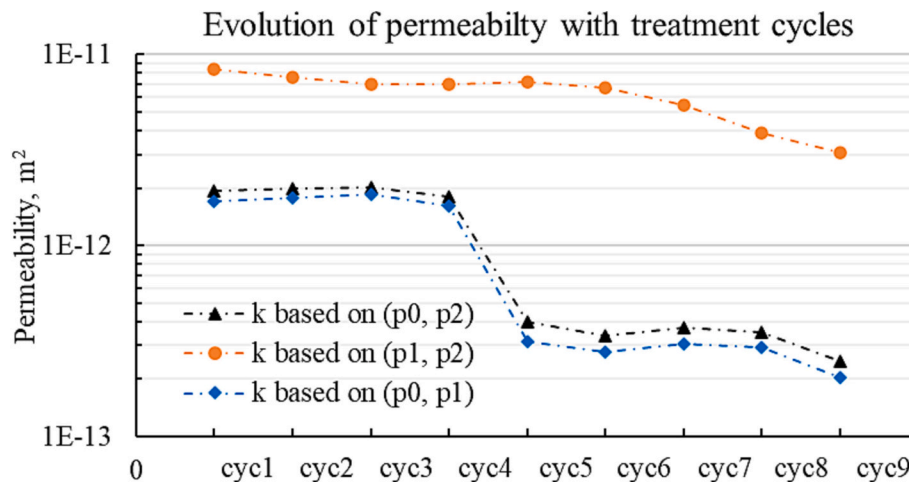

Fig. 8. Permeability evolution of the soils in the radial flow cells as a function of MICP treatment cycle, which were calculated based on different pressures monitored at the injection well (p_0), the sampling port (p_1), and outer boundary (p_2).
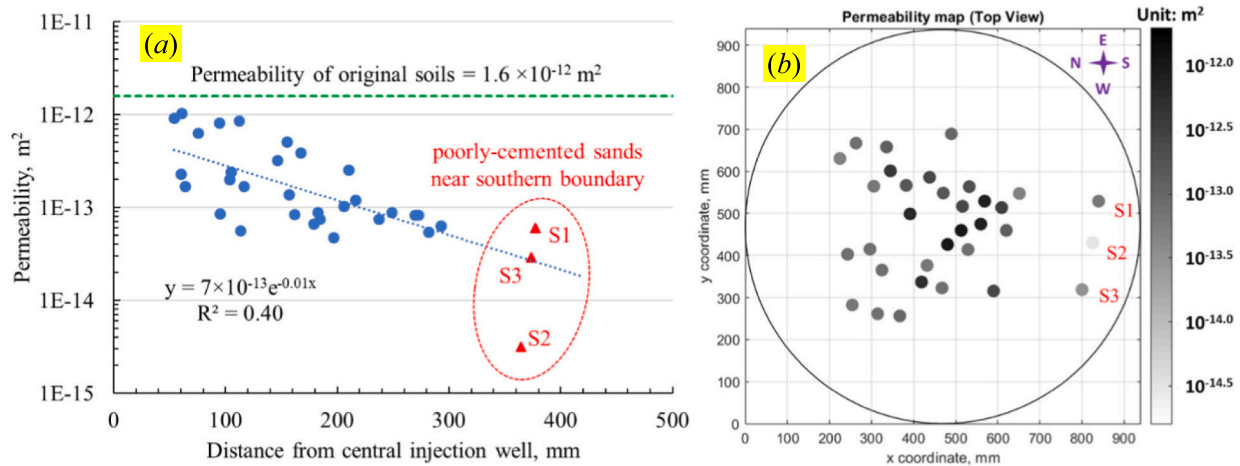
Fig. 9. (*a*) Permeability of the post-treated cores (blue solid dots) and three poorly-cemented sand samples near the southern boundary (red solid triangles), plotted against distance to the central injection well; (*b*) 2-D spatial distribution of the cores used for permeability measurements (a). (For interpretation of the references to colour in this figure legend, the reader is referred to the web version of this article.)

for the delivery of bacteria and cementing solutions, and leaving the soils in this zone poorly cemented. In field conditions, where the overburden pressure is higher (with depth), fine migration may be less likely to occur.

4.4. Unconfined compressive strength

The unconfined compressive strengths (UCSs) of the MICP-cemented medium-graded very gravelly sand, together with UCS values from previous studies in the literature (Al Qabany and Soga, 2013; Cheng et al., 2013, 2017; Cui et al., 2017; Gowthaman et al., 2019; Li et al., 2017, 2018; Mahawish et al., 2016; Rowshanbakht et al., 2016; van Paassen et al., 2010; Wu et al., 2020) are plotted against the weight percentage of calcium carbonate in Fig. 10. After nine cycles of MICP treatment, UCS values of the MICP-treated very gravelly sand from the radial flow experiment were determined ranging between 2.6 and 7.4 MPa, while their $CaCO_3$ contents ranged from 0.092 to 0.151. As expected, there is a positive correlation between UCS and calcium carbonate content, since crystalized calcium carbonate serves as the cementitious material that bonds soil grains together. When compared with MICP-cemented sands from previous studies which were based on either uniformly-graded or poorly-graded non-gravel containing sands

according to BS EN ISO 14688-2:2018, the UCS values for the cemented medium-graded very gravelly sand in this study (Fig. 10) are higher than would be expected based on their $CaCO_3$ content. In this sense, better graded sands tend to have a higher cementation efficiency. Factors controlling the cementation efficiency of MICP are discussed in Section 5.2.

The 2-D spatial distribution of UCS of the drilled core samples is shown in Fig. 11 and is clearly spatially heterogeneous. Fig. 11 also schematically marks the poorly-cemented regions where no intact cores were drilled in the flow cell. The soil in this study contained a very wide range of grain sizes that were angular in shape, including both fines and angular granular particles (as will be shown in the SEM images). The pre-existing and/or hydraulically-induced non-uniform flow field likely contributed to the spatial heterogeneity in UCS values of cores sampled from the flow cell. For example, the soils near the southern boundary (S1, S2, S3, S4) were poorly-cemented ($CaCO_3$ content: 1.7–2.1%), possibly due to fines migration creating a region of low permeability as detailed in Section 4.4, which limited the accessibility of the bacteria and cementing solution to this region. Despite the spatial heterogeneity of the soil, an overall strong cementation was achieved in most regions with UCS values ranging between 2.6 and 7.4 MPa throughout the remainder (>71%, as estimated from Fig. 11) of the flow cell.
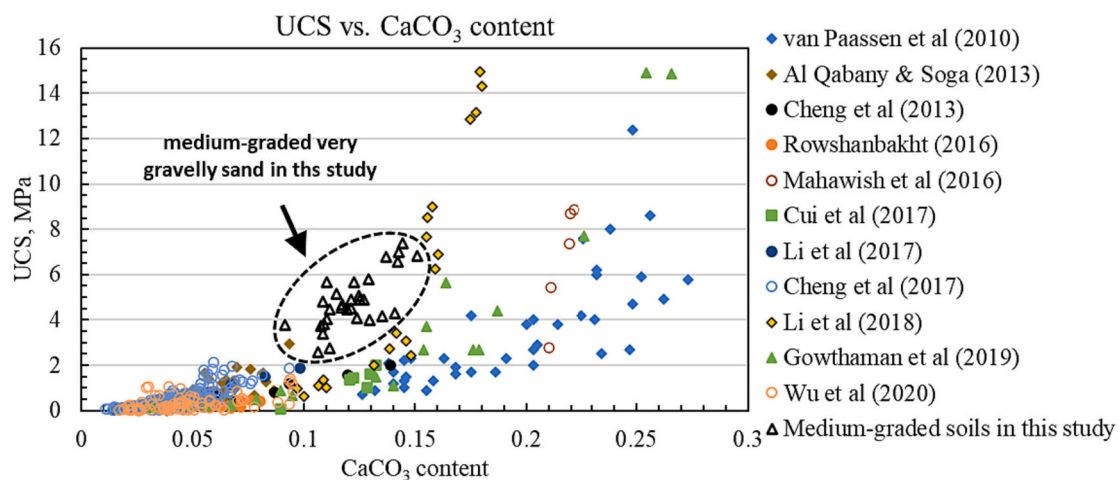

Fig. 10. Unconfined compressive strength (UCS) plotted against $CaCO_3$ content for the biocemented soils in this study and from the literature (Al Qabany and Soga, 2013; Cheng et al., 2013, 2017; Cui et al., 2017; Gowthaman et al., 2019; Li et al., 2017, 2018; Mahawish et al., 2016; Rowshanbakht et al., 2016; van Paassen et al., 2010; Wu et al., 2020).
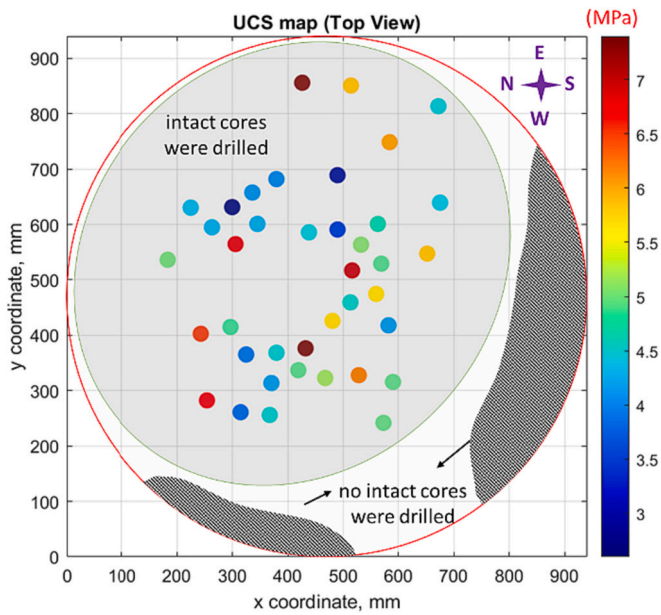
Fig. 11. 2-D spatial distribution UCS of the post-treated medium-graded very gravelly sand in the flow cell.

4.5. Triaxial tests

Fig. 12 shows the drained triaxial test results for the two cores samples (#1 and #2) and the untreated soil, under an effective confining stress of 100 kPa. The two treated cores #1 and #2 had a peak deviatoric strength of 5.9 MPa and 3.7 MPa, respectively, at an axial strain of ~1.3%. As expected, the untreated soil had a much lower peak deviatoric stress (0.5 MPa) at a higher axial strain (2.6%), demonstrating that MICP treatment has enhanced the peak deviatoric stress achieved at this confining stress. The two treated cores exhibited more brittle behaviour with higher stiffness than the untreated sample. After the peak strength, the deviatoric stresses of the two treated cores started to drop but both were maintained at a higher value than the untreated soil, thus suggesting that the bio-cemented cores had a higher residual strength due to the carbonate precipitation. Fig. 12 (b) shows the curves of volumetric strain versus axial strain (positive sign denotes contraction). The three samples exhibited an initial increase in volumetric strain (i.e. contraction) followed by a decrease in volumetric strain (i.e. dilation), with final dilations, at an axial strain of 15%, of 8.3% (sample #1), 7.3% (sample #2) and 1.6% (untreated sample). Other studies (Montoya et al., 2015; Nafisi et al., 2020; Wu et al., 2021) also demonstrated the enhanced shear strength and the dilative behaviour of biocemented soils, but the extents of strength enhancement and dilation of the bio-cemented soils at a confining stress of 100 kPa are smaller than the biocemented gravelly sands in this study. This likely results from (1) $CaCO_3$ content of the biocemented gravelly sands in this study (i.e. 9–15%) is higher than in other studies (Montoya et al., 2015; Nafisi et al., 2020); (2) at similar $CaCO_3$ content (9–15%), the presence of more angular shaped grains (as shown later by the SEM images) with a broader size distribution (uniformity coefficient ~ 10) are prone to roll over during shearing and hence promote a higher strength and more dilation than the biocemented poorly-graded sand (shear strength <3.3 MPa, dilation <5% at $CaCO_3$ content of 12%) by Wu et al. (2021). After the triaxial test, a shear band was clearly visible in the two treated core samples in Fig. 12 (c), whilst bulging deformation was observed for the untreated sample. The high peak strength, the high stiffness and dilation, plus the formation of shear bands in the two treated core samples, as shown in Fig. 12a, b, & c, demonstrate that these cores were well-cemented after 9 cycles of MICP treatment.
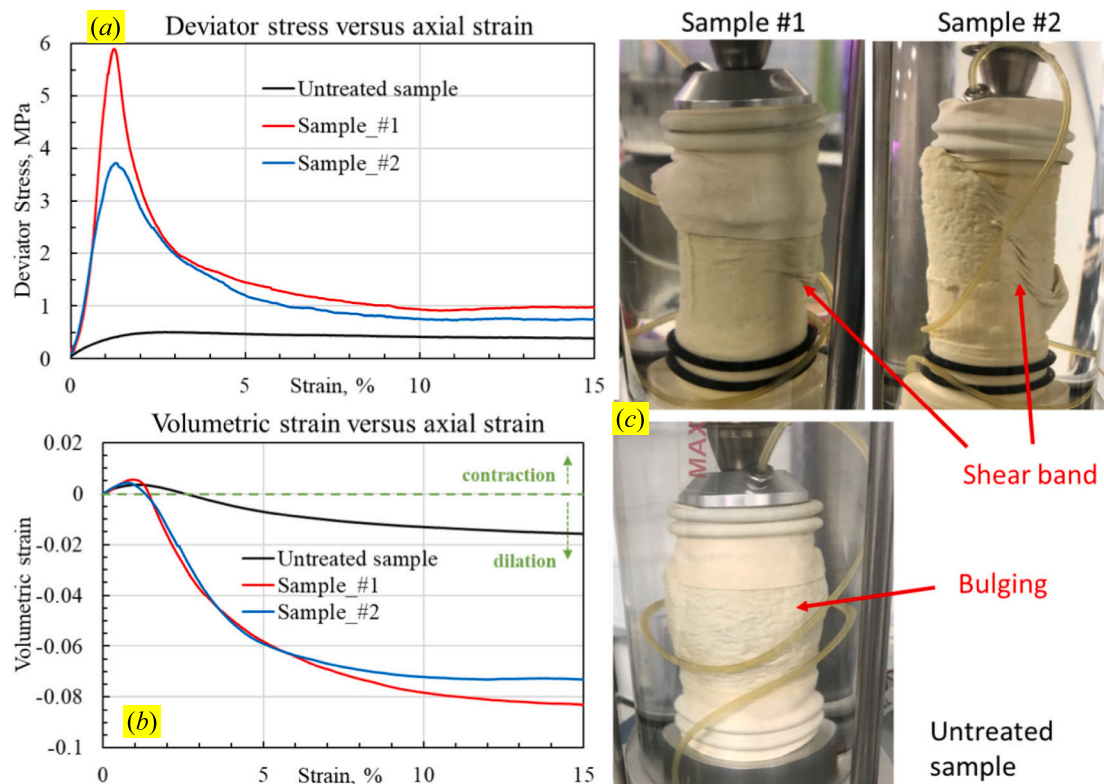

Fig. 12. Triaxial tests of the two treated samples (#1, #2) and an untreated sample under consolidation-drainage conditions (effective confining stress of 100 kPa). (a) deviatoric stress and (b) volumetric strain versus axial strain during the shear stage; (c) images of the post-failed samples.

4.6. SEM analysis and X-CT imaging

Fig. 13 (*a*) shows the backscattered electron (BSE) images of the polished specimen with soil grains (blue arrows), resin epoxy (black arrows), and CaCO$_3$ precipitated between soil grains (red arrows), as identified by the EDS spectra in Fig. 13 (*b*). Fig. 13 (*c-f*) also show angular soil grains with broad particle sizes. The precipitated calcite is shown to be coating grains, filling pore space and also bridging between two or more grains.

A BSE image with high magnification is shown in Fig. 14 (*a,b*) (as well as SI Fig. S12*b*) which shows several layers of calcite extending from the surface of the grains to the middle of the pore. Similar layers are observed in the SEM images of (Tobler et al., 2018) and (Ismail et al., 2002). The generation of the calcite layers is closely linked with the growth of calcite crystals in each treatment cycle. Round cavities, with diameters close to the cross section of a single bacterial cell (~0.5–1

μm), are also clearly visible within the calcite crystals. Calcite crystals likely nucleated on the bacterial cell surfaces and then extended via crystal growth, leaving individual bacteria cells embedded within the calcite crystals (Stocks-Fischer et al., 1999). During subsequent treatment cycles, fresh bacteria (and calcium) are added, these settle on the surface of the crystals, and the process repeats, producing a new calcium carbonate layer with each additional treatment cycle.

Fig. 15 shows secondary electron images of the unpolished sample (without resin epoxy) for the core sample with the highest UCS. Two types of calcite precipitation are visible, depending on location: calcium carbonate crystals coating the surface of the soil grains (Fig. 15*a* & *b*) and calcium carbonate bridging two or more soil grains (Fig. 15*c* & *d*). Both types of calcium carbonate precipitation tend to reduce the permeability by either decreasing pore volume or narrowing pore throats. This is the main cause of permeability reduction in the core samples (Figs. 8 and 9) after 9 cycles of MICP treatment. Sample strength
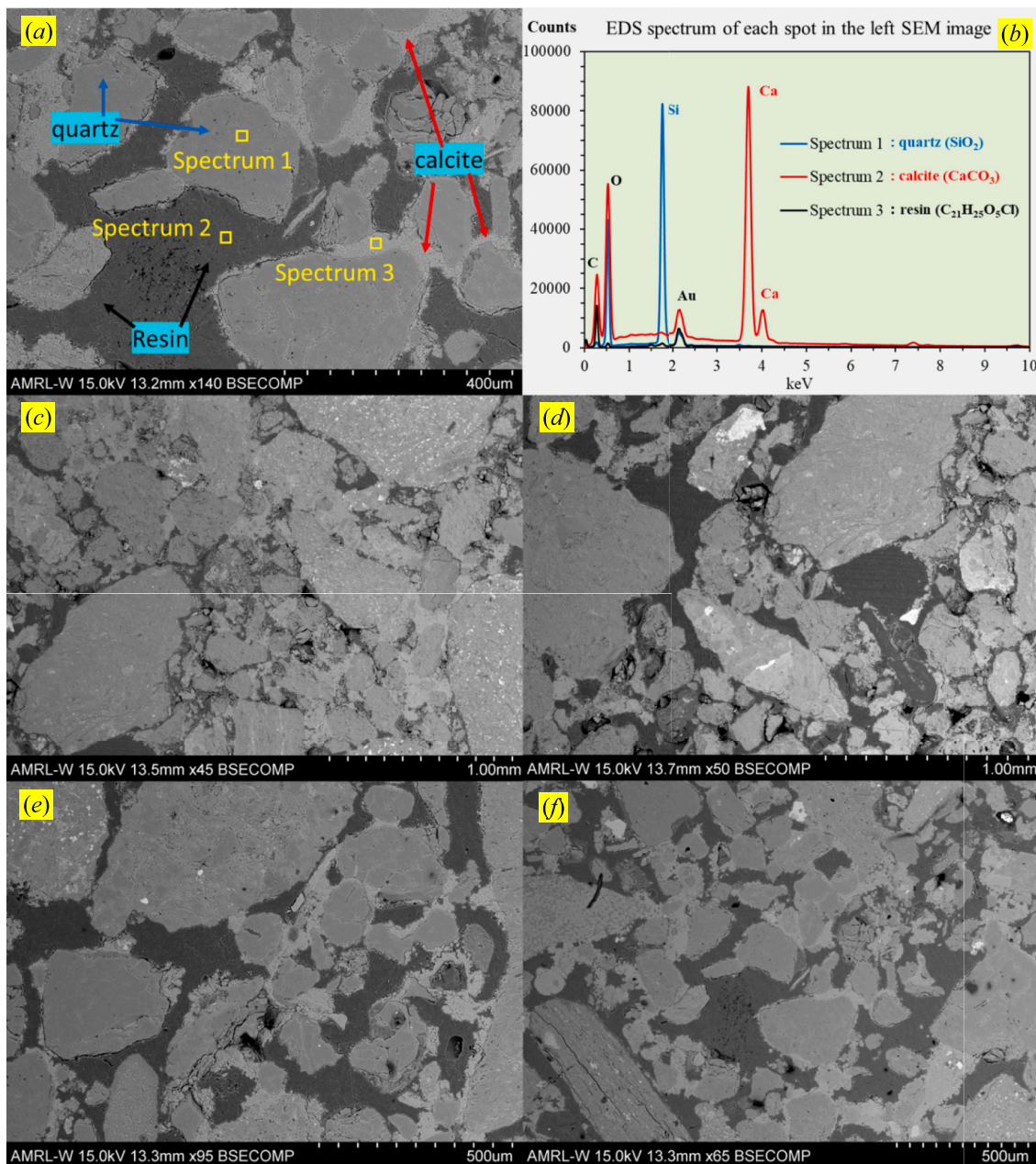

Fig. 13. (*a-e*) Backscattered electron (BSE) images of the polished specimen showing angular grains (dark blue arrow) with various sizes, resin epoxy (white arrow), and precipitated calcite (yellow arrow) near the grain-to-grain contact points. (*f*) voids filled with precipitated calcite with one fine particle enveloped inside.
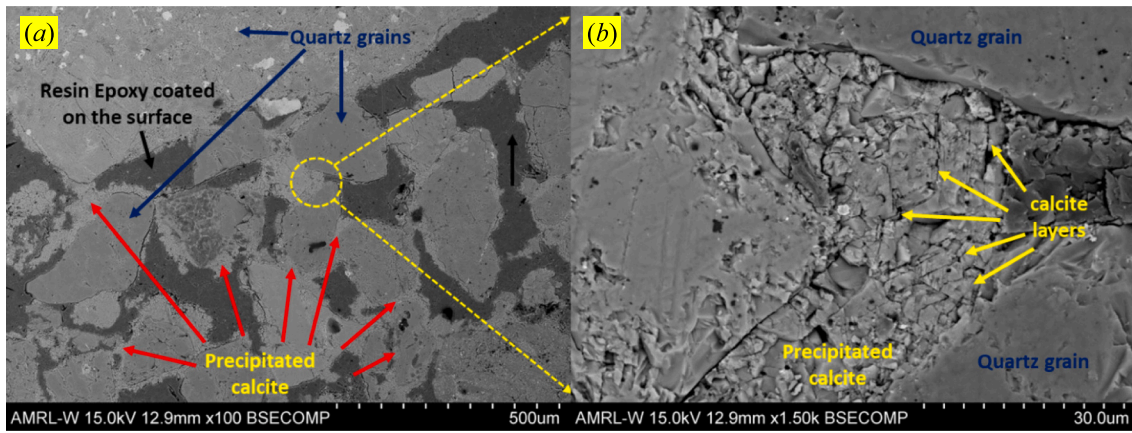
Fig. 14. (a) BSE image of another spot of the polished specimen; (b) BSE image with higher magnification (×1.5 K) showing precipitated calcite bridging two grains and exhibiting several layers of precipitated calcite extended from the contact point toward the middle; the precipitated calcite also shows cavities left by embedded bacterial cells (~0.5–1 μm).

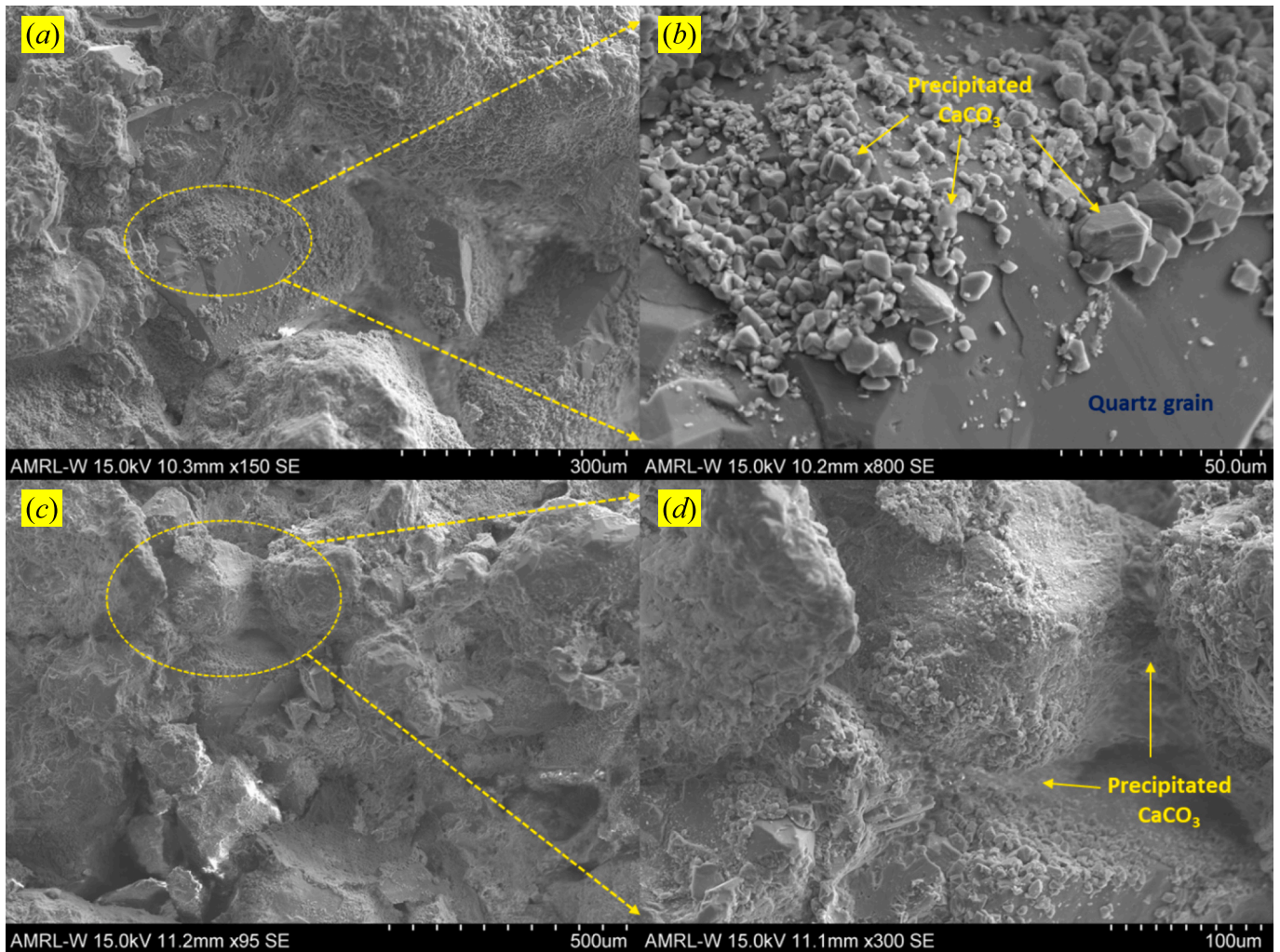**Fig. 15.** (a) Secondary electron images of the unpolished sample (with the strongest UCS) showing calcite precipitation coated on the surface of the soil grains (a & b), and bridging soil grains (c & d).

is related to the calcite bridging between grains at, or near to, grain-to-grain contact points, it is not dependent on surface coating unless the void is fully filled with calcite, in which case surface coating contributes to bridging. A 3-dimensional DEM model by Wu et al. (2023) also demonstrated that the mechanical properties and failure behaviours of biocemented sands are highly dependent on the precipitation patterns, which are classified into effective or partially effective bonding, surface coating, and pore filling. It is the effective (or partially effective)

bonding that mainly controls the mechanical strength and stiffness.

Fig. 16 (b,c) shows a central slice from the CT scan of a core drilled through the effluent port. Within this core, regions with well-cemented, and with less well-cemented, grains are visible producing heterogeneity in the final cemented sample. Due to the heterogeneity of the soil and the similarity of the X-ray attenuation values for calcite and quartz, it is difficult to segment the CT images without introducing bias. Therefore, 3D quantitative analysis of the precipitated calcite is not included here.

5. Discussion and implication

5.1. Tracer and bacteria transport

In the 3rd stage of the column breakthrough test (Fig. 5b), the injection of 5PV tap water induced bacterial release. Considering the classical DLVO theory of colloid stability (Derjaguin and Landau, 1941; Verwey and Overbeek, 1955), this release of bacteria is possibly due to the appearance of a secondary minimum (i.e. a weak attractive force between bacteria and grain surfaces) and/or energy repulsion (i.e. repulsive force between bacteria and grain surfaces) under the elution of tap water with a much lower ionic strength (Choi et al., 2017). This provides direct experimental evidence that tap water with a much lower ionic strength than the injected bacterial solution can be used for well cleaning to avoid clogging. Indeed, after 9 cycles of MICP treatment, soils near the central injection well within a diameter of ~6 cm were poorly cemented, as can be seen from the top view of the radial flow cell in SI Fig. S13.

The approximate agreement between the modelled and observed tracer breakthrough (Fig. 6a & b) indicates that there was effective delivery of the bacteria and the cementing solution near the effluent sampling port. However, preferential flow paths in the radial flow cell still existed which caused the tracer to breakthrough later than predicted at the effluent sampling port. The difference between the overall bulk permeability of the radial flow cell (Fig. 8), as calculated from pressure difference between the injection well and sampling port/outer boundary, and the average soil permeability calculated for the soil between the sampling port and outer boundary, also indicates that flow is not uniformly radial. These preferential flow paths may become less pronounced with increasing numbers of cycles: the initial soil body was heterogeneous upon emplacement, causing a greater delivery of bacteria

and cementing solution to regions of high permeability; this will result in a higher rate of calcium carbonate precipitation in these initially permeable regions, thus reducing the permeability more rapidly than elsewhere and potentially resulting in more uniform treatment during later cycles.

5.2. Factors controlling cementation efficiency

The role of particle size on cementation efficiency has been explored previously. (Ismail et al., 2002) found that MICP treated fine-grained sands had a higher strength than coarse grained sands due to their higher density of grain contact points. Note, however, that total calcite precipitation also increased with reduced particle size (Ismail et al., 2002), since the total surface area of the grains is increased, thus it is difficult to say that grains with a finer size enhance the cementation efficiency (i.e. are stronger for a given mass of calcite precipitation). In fact, (Terzis and Laloui, 2018) found that medium-grained bio-cemented sands corresponded to higher compressive strengths than fine-grained sands for the same mass of calcite precipitated. Apart from the particle size, the response of soils to calcite treatment is influenced by other factors, as summarized by (Ismail et al., 2002), including intrinsic strength of the host grains, density of the soil matrix, particle shape and the surface condition of host grains. Possible mechanisms for the higher cementation efficiency observed in this study (Fig. 10) are summarized as follows.

Firstly, the field soils in this study consisted of 31.4% gravels and 64.7% sands with angular shapes, as shown by the SEM and CT images in Figs. 13 and 16, respectively. Ismail et al. (2002) found that spherical/rounded particles tend to be exposed to more contact points, less stress concentration, and therefore better cementation efficiency, however, we argue that soils with angular particles tend to have a better cementation efficiency due to the greater particle interlocking effect (Alshibli et al., 2016; Guo and Su, 2011) and longer contact interfaces for cementation (Xiao et al., 2019b). (Xiao et al., 2019a) studied the effect of particle shape on biocemented glass beads, and found that angular glass beads resulted in a higher biocemented strength and stiffness than in round beads, despite a slightly lower mass of calcite precipitated. This occurs because the effective contact interface between angular particles is larger than that between rounded particles (Xiao et al., 2019b). Therefore, bio-cemented soils with angular and randomly-oriented particles
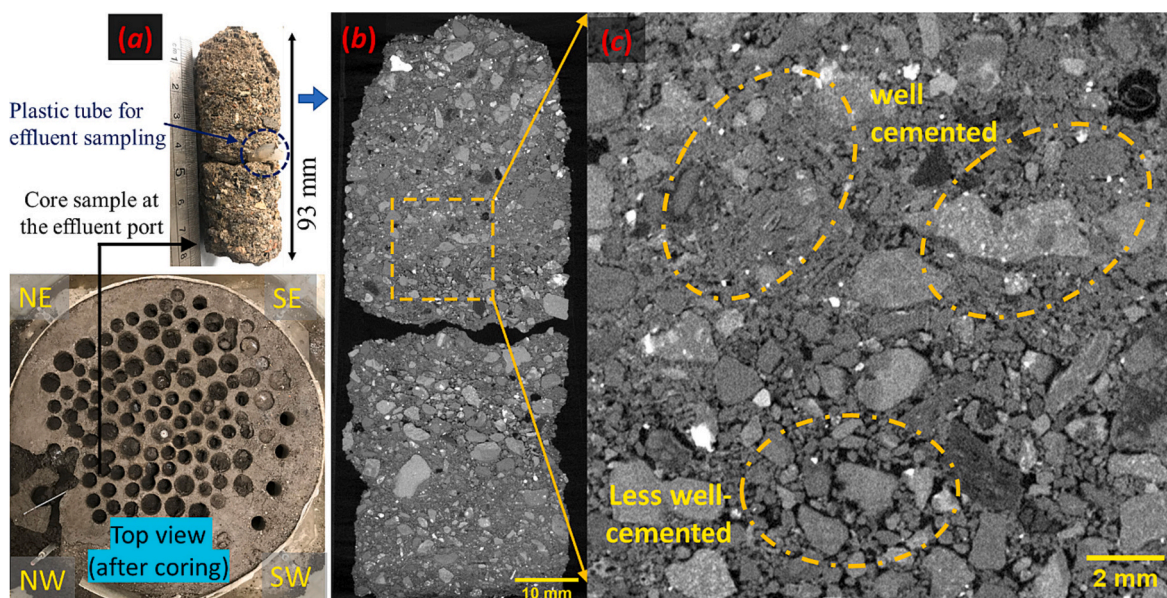

Fig. 16. CT images showing heterogeneously cemented soils cored at the effluent sampling port after MICP treatment. (a) core sample drilled at the effluent sampling port; (b) one CT slice showing bio-cemented sands with different particle sizes; (c) zoomed slice showing well-cemented and pooly-cemented grains with angular shape and various sizes.

tends to have better cementation efficiency (i.e. higher strengths at a given calcite content) as shown in Fig. 10.

Secondly, the sandy soils in other studies listed in Fig. 10 were either uniformly-graded or poorly-graded (Al Qabany and Soga, 2013; Cheng et al., 2013, 2017; Cui et al., 2017; Gowthaman et al., 2019; Li et al., 2017, 2018; Mahawish et al., 2016; Rowshanbakht et al., 2016; van Paassen et al., 2010; Wu et al., 2020). The medium-graded nature and the presence of small-sized sands, silts and clays in this study contributes to a relatively high degree of compactness of the soil skeleton (or relative density). This significantly increases the number of grain-to-grain contact points (Zamani and Montoya, 2019) and promotes bacterial straining at crevices and constrictions, thus contributing to an effective bridging/bonding between grains and increasing the cementation efficiency. This finding is consistent with previous small-scale laboratory studies (Al Qabany, 2011; Rowshanbakht et al., 2016; Zamani and Montoya, 2019) who also found that higher relative soil density and more contact points corresponded to a higher cementation efficiency of MICP, although the total amount of calcite precipitated was lower due to the lower void ratio. In engineering practice, soil compaction measures could increase the relative density and hence increase the cementation efficiency of MICP treatment (Tang et al., 2020).

5.3. Implications on field soil improvement

Major challenges to large-scale soil improvement, as outlined by (El Mountassir et al., 2018), include prevention of clogging near the injection well, optimization of the treatment strategy to minimize cost and carbon footprint, and the achievement of a relatively homogeneous calcite precipitation. As discussed in Section 5.1, well-cleaning by flushing a small amount of tap water (with a low ionic content) was sufficient to avoid clogging induced by MICP near the injection zone, since it caused bacterial release and impeded carbonate precipitation at the injection well. In terms of lowering the cost of bio/chemical materials and their carbon footprint, several measures could be taken including using the recirculation injection method to enhance the overall bacterial deposition efficiency (Martinez et al., 2013) or calcium conversion efficiency (Wu et al., 2020), stimulating native or artificially injected ureolytic microorganisms (Gomez et al., 2017a, 2017b), extracting soluble calcium sources from natural materials (Choi et al., 2016; Liu et al., 2018), etc. Our experimental results suggest that increased soil compaction, prior to treatment, may also increase the cementation efficiency, and hence reduce the number of MICP cycles required to achieve a target strength.

Perhaps the greatest challenge of MICP application in man-made geotechnical structures or natural in situ soil deposits is the achievement of homogeneous calcite precipitation within the entire target zone. Specifically, the presence of soil heterogeneity produces a non-uniform flow field and will result in uneven delivery of the treatment fluids (bacterial solution and cementing solution). Whilst the existence of fines and small-sized sands in medium-graded soils will promote more grain-to-grain contact area, deposits with a wide range of grain sizes are also likely to exhibit more spatial heterogeneity. Further, during injection, fines may migrate away from the injection point from the more permeable zones, and subsequently filter out in lower permeability regions, resulting in increased spatial heterogeneity. Non-uniform flow poses a challenge for the effective delivery of bacteria and treatment reagents to lower permeability zones, thus impairing the overall treatment efficiency of MICP in the field. Nevertheless, our study demonstrates that in a medium-graded very gravelly sand (i.e. mixture of 31.4% gravels, 64.7% sands, and 3.9% fines) at least 71% of the soil can be well-treated based on a two-phase grouting approach, i.e. Phase 1. augmenting bacterial solution, and Phase 2. circulation of 0.5 M cementing (CaCl$_2$ & Urea) solution. In practice, the efficacy of MICP in non-uniform heterogeneous soils will depend on the geometry of the high and low permeability regions, as well as on the absolute range of the permeability values. For example, if a region of very high or very low

permeability is geometrically isolated, as in the case of a void, a clay lens or a region of high clay content, the surrounding soil will be successfully treated as long as the volume of the void/lens is small in comparison to the total treatment volume. In such cases, the effect on the bulk soil strength after treatment will be relatively minor, as demonstrated here. However, if a high permeability feature, such as a gravel layer, is geometrically continuous over a large region, it will inhibit bulk treatment of the soil. This effect is reported in a layered soil by (Zeng et al., 2021a) where MICP treatment fluids travelled long distances from the injection point within the permeable layers, resulting in treatment of only ~5% of the target soil volume. In such cases, permeable layers should be identified and grouted prior to MICP treatment of the bulk soil, in order to reduce their permeability e.g. with cementitious grout or colloidal silica (Pagano et al., 2022; Pedrotti et al., 2020). Thus, successful MICP treatment in heterogeneous soils will rely on a well-designed and well-executed site investigation programme that can identify, a priori, the geometry of any significant high or low permeability features within the soil body, and thus inform the final MICP treatment strategy.

6. Conclusion

In this study, MICP treatment of medium-graded very gravelly sand was performed within a meter-scale radial flow cell (diameter ~ 1 m, thickness ~ 0.15 m). The unconfined compressive strength of the resulting biocemented soil, as tested on cored samples, ranged between 2.6 and 7.4 MPa after 9 cycles of treatment. Consolidated-drained triaxial tests on two cores showed a peak deviatoric stress at failure of 5.9 MPa and 3.7 MPa under an effective confining stress of 100 kPa. The two biocemented cores also behaved a strong dilative behaviour with narrow shear band formed after failure. Comparison with the untreated sand (tested at the same confining stress) indicated that MICP treatment enhanced the shear strength and brittleness of the medium-graded soil.

Transport modelling results based on column breakthrough tests and radial flow tests suggest that there was effective delivery of bacteria and chemicals (i.e. urea and CaCl$_2$) in the radial flow cell. Monitoring of the aqueous chemistry of the effluent samples (i.e. electrical conductivity and pH) taken from the sampling port during treatment cycles confirmed that bio-cementation was occurring. Transport modelling and monitoring of the electrical conductivity showed that measured tracer breakthrough at the effluent sampling point was slightly later than predicted, indicating the presence of a non-uniform radial flow field and the existence of some preferential flow paths. A small amount of tap water flushing was successful at preventing clogging near the injection well.

The overall permeability of the soil in the radial flow cell dropped by one order of magnitude after 9 cycles of MICP treatment due to calcite precipitation. The local permeability in the radial flow cell was spatially heterogeneous, with the permeability of the drilled cores decreasing with distance from the central injection well. This was likely due to the migration of fines during injection, from the central injection point to the outer boundary. Despite the spatial heterogeneity of permeability in the flow cell, a biocemented sand (UCS = 2.6–7.4 MPa) was achieved in at least 71% of the meter-scale cell.

The cementation efficiency of the medium-graded very gravelly sand treated in this study was relatively high when compared to studies in the literature that mainly treat uniform/poorly graded sand i.e. higher strengths were achieved here for the same calcite content. SEM and CT images show that this can be attributed to more calcite bridging between grains, due to the higher initial density of grain-to-grain contact points in medium-graded soil, and a high grain angularity which resulted in particle interlocking and longer grain-to-grain contact surfaces.

CRediT authorship contribution statement

Guijie Sang: Conceptualization, Data curation, Formal analysis,

Investigation, Methodology, Software, Visualization, Writing – original draft. **Rebecca J. Lunn:** Conceptualization, Funding acquisition, Investigation, Methodology, Project administration, Resources, Supervision, Validation, Writing – review & editing. **Grainne El Mountassir:** Conceptualization, Investigation, Methodology, Supervision, Validation, Writing – review & editing. **James M. Minto:** Conceptualization, Investigation, Methodology, Supervision, Validation, Writing – review & editing.

Declaration of Competing Interest

The authors declare that they have no known competing financial interests or personal relationships that could have appeared to influence the work reported in this paper.

Data availability

Data will be made available on request.

Acknowledgments

Appendix A. Supplementary data

Supplementary data to this article can be found online at https://doi.org/10.1016/j.enggeo.2023.107275.

References

Al Qabany, A.A.A., 2011. Microbial Carbonate Precipitation in Soils. University of Cambridge.

Al Qabany, A., Soga, K., 2013. Effect of Chemical Treatment used in MICP on Engineering Properties of Cemented Soils, 63, pp. 331–339. https://doi.org/10.1680/GEOT.SIP13.P.022.

Alshibli, K.A., Jarrar, M.F., Druckrey, A.M., Al-Raoush, R.I., 2016. Influence of particle morphology on 3D kinematic behavior and strain localization of sheared sand. J. Geotech. Geoenviron. Eng. 143, 04016097. https://doi.org/10.1061/(ASCE)GT.1943-5606.0001601.

BSI, 2018. BS EN ISO 14688-2:2018. Geotechnical Investigation and Testing. Identification and Classification of Soil - Principles for a Classification.

Chae, S.H., Chung, H., Nam, K., 2021. Evaluation of microbially induced calcite precipitation (MICP) methods on different soil types for wind erosion control. Environ. Eng. Res. 26, 1–6. https://doi.org/10.4491/EER.2019.507.

Cheng, L., Cord-Ruwisch, R., 2014. Upscaling effects of soil improvement by microbially induced calcite precipitation by surface percolation. Geomicrobiol J. 31, 396–406.

Cheng, L., Cord-Ruwisch, R., Shahin, M.A., 2013. Cementation of sand soil by microbially induced calcite precipitation at various degrees of saturation. Can. Geotech. J. 50, 81–90. https://doi.org/10.1139/CGJ-2012-0023/ASSET/IMAGES/LARGE/CGJ-2012-0023F16.JPEG.

Cheng, L., Shahin, M.A., Asce, M., Mujah, D., Scholar, P., 2017. Influence of key environmental conditions on microbially induced cementation for soil stabilization. J. Geotech. Geoenviron. Eng. 143 https://doi.org/10.1061/(ASCE)GT.1943-5606.0001586.

Cheng, Y.J., Tang, C.S., Pan, X.H., Liu, B., Xie, Y.H., Cheng, Q., Shi, B., 2021. Application of microbial induced carbonate precipitation for loess surface erosion control. Eng. Geol. 294, 106387 https://doi.org/10.1016/J.ENGGEO.2021.106387.

Choi, S.-G., Wu, S., Chu, J., 2016. Biocementation for sand using an eggshell as calcium source. J. Geotech. Geoenviron. Eng. 142, 06016010. https://doi.org/10.1061/(ASCE)GT.1943-5606.0001534.

Choi, N.-C., Choi, J.-W., Kwon, K.-S., Lee, S.-G., Lee, S., 2017. Quantifying bacterial attachment and detachment using leaching solutions of various ionic strengths after bacterial pulse. AMB Express 71 (7), 1–9. https://doi.org/10.1186/S13568-017-0340-2, 2017.

Cui, M.J., Zheng, J.J., Zhang, R.J., Lai, H.J., Zhang, J., 2017. Influence of cementation level on the strength behaviour of bio-cemented sand. Acta Geotech. 12, 971–986. https://doi.org/10.1007/S11440-017-0574-9/FIGURES/17.

DeJong, J.T., Fritzges, M.B., Nüsslein, K., 2006. Microbially induced cementation to control sand response to undrained shear. J. Geotech. Geoenviron. Eng. 132, 1381–1392. https://doi.org/10.1061/(ASCE)1090-0241(2006)132:11(1381).

Derjaguin, B., Landau, L., 1941. Theory of the stability of strongly charged lyophobic sols and of the adhesion of strongly charged particles in solutions of electrolytes. Prog. Surf. Sci. 43, 30–59. https://doi.org/10.1016/0079-6816(93)90013-L.

El Mountassir, G., Minto, J.M., van Paassen, L.A., Salifu, E., Lunn, R.J., 2018. Applications of microbial processes in geotechnical engineering. Adv. Appl. Microbiol. 104, 39–91. https://doi.org/10.1016/BS.AAMBS.2018.05.001.

Gomez, M.G., Martinez, B.C., DeJong, J.T., Hunt, C.E., deVlaming, L.A., Major, D.W., Dworatzek, S.M., 2015. Field-scale bio-cementation tests to improve sands. Proc. Inst. Civ. Eng.: Ground Improv. 168, 206–216. https://doi.org/10.1680/grim.13.00052.

Gomez, M.G., Anderson, C.M., Graddy, C.M.R., DeJong, J.T., Nelson, D.C., Ginn, T.R., 2017a. Large-scale comparison of bioaugmentation and biostimulation approaches for biocementation of sands. J. Geotech. Geoenviron. Eng. 143, 04016124. https://doi.org/10.1061/(ASCE)GT.1943-5606.0001640.

Gomez, M.G., Graddy, C.M.R., DeJong, J.T., Nelson, D.C., Tsesarsky, M., 2017b. Stimulation of native microorganisms for biocementation in samples recovered from field-scale treatment depths. J. Geotech. Geoenviron. Eng. 144, 04017098. https://doi.org/10.1061/(ASCE)GT.1943-5606.0001804.

Gowthaman, S., Iki, T., Nakashima, K., Ebina, K., Kawasaki, S., 2019. Feasibility study for slope soil stabilization by microbial induced carbonate precipitation (MICP) using indigenous bacteria isolated from cold subarctic region. SN Appl. Sci. 1, 1–16. https://doi.org/10.1007/S42452-019-1508-Y/FIGURES/18.

Guo, P., Su, X., 2011. Shear Strength, Interparticle Locking, and Dilatancy of Granular Materials, 44, pp. 579–591. https://doi.org/10.1139/T07-010.

Head, K.H., 1980. Manual of Soil Laboratory Testing. Pentech press London.

Ismail, M.A., Joer, H.A., Randolph, M.F., Meritt, A., 2002. Cementation of porous materials using calcite. Geotechnique 52, 313–324. https://doi.org/10.1680/geot.2002.52.5.313.

Li, M., Wen, K., Li, Y., Zhu, L., 2017. Impact of Oxygen Availability on Microbially Induced Calcite Precipitation (MICP) Treatment, 35, pp. 15–22. https://doi.org/10.1080/01490451.2017.1303553.

Li, D., Tian, K., Zhang, H., Wu, Y., Nie, K., Zhang, S., 2018. Experimental investigation of solidifying desert aeolian sand using microbially induced calcite precipitation. Constr. Build. Mater. 172, 251–262. https://doi.org/10.1016/J.CONBUILDMAT.2018.03.255.

Liu, L., Liu, H., Xiao, Y., Chu, J., Xiao, P., Wang, Y., 2018. Biocementation of calcareous sand using soluble calcium derived from calcareous sand. Bull. Eng. Geol. Environ. 77, 1781–1791. https://doi.org/10.1007/S10064-017-1106-4/FIGURES/19.

Liu, B., Xie, Y.H., Tang, C.S., Pan, X.H., Jiang, N.J., Singh, D.N., Cheng, Y.J., Shi, B., 2021. Bio-mediated method for improving surface erosion resistance of clayey soils. Eng. Geol. 293, 106295 https://doi.org/10.1016/J.ENGGEO.2021.106295.

Mahawish, A., Bouazza, A., Gates, W.P., 2016. Biogrouting coarse materials using soil-lift treatment strategy. Can. Geotech. J. 53, 2080–2085. https://doi.org/10.1139/CGJ-2016-0167/ASSET/IMAGES/LARGE/CGJ-2016-0167F6.JPEG.

Martinez, B.C., DeJong, J.T., 2009. Bio-Mediated Soil Improvement: Load Transfer Mechanisms at the Micro- and Macro- Scales, pp. 242–251. https://doi.org/10.1061/41025(338)26.

Martinez, B.C., DeJong, J.T., Ginn, T.R., Montoya, B.M., Barkouki, T.H., Hunt, C., Tanyu, B., Major, D., 2013. Experimental optimization of microbial-induced carbonate precipitation for soil improvement. J. Geotech. Geoenviron. Eng. 139, 587–598. https://doi.org/10.1061/(ASCE)GT.1943-5606.0000787.

Minto, J.M., MacLachlan, E., El Mountassir, G., Lunn, R.J., 2016. Rock fracture grouting with microbially induced carbonate precipitation. Water Resour. Res. 52, 8827–8844. https://doi.org/10.1002/2016WR018884.

Minto, J.M., Lunn, R.J., El Mountassir, G., 2019. Development of a reactive transport model for field-scale simulation of microbially induced carbonate precipitation. Water Resour. Res. 55, 7229–7245.

Mobley, H.L.T., Island, M.D., Hausinger, R.P., 1995. Molecular biology of microbial ureases. Microbiol. Rev. 59, 451–480. https://doi.org/10.1128/MR.59.3.451-480.1995.

Montoya, B.M., Dejong, J.T., 2013. Healing of biologically induced cemented sands. Geotech. Lett. 3, 147–151. https://doi.org/10.1680/GEOLETT.13.00044/ASSET/IMAGES/SMALL/GEOLETT3-147-F3.GIF.

Montoya, B.M., Asce, M., Dejong, J.T., 2015. Stress-strain behavior of sands cemented by microbially induced calcite precipitation. J. Geotech. Geoenviron. Eng. 141, 04015019. https://doi.org/10.1061/(ASCE)GT.1943-5606.0001302.

Nafisi, A., Asce, S.M., Montoya, B.M., Asce, M., Evans, T.M., Asce, A.M., 2020. Shear strength envelopes of biocemented sands with varying particle size and cementation level. J. Geotech. Geoenviron. Eng. 146, 04020002. https://doi.org/10.1061/(ASCE)GT.1943-5606.0002201.

Pagano, A.G., El Mountassir, G., Lunn, R.J., 2022. Performance of colloidal silica grout at elevated temperatures and pressures for cement fracture sealing at depth. J. Pet. Sci. Eng. 208, 109782.

Pedrotti, M., Wong, C., El Mountassir, G., Renshaw, J.C., Lunn, R.J., 2020. Desiccation behaviour of colloidal silica grouted sand: a new material for the creation of near surface hydraulic barriers. Eng. Geol. 270, 105579.

Rowshanbakht, K., Khamehchiyan, M., Sajedi, R.H., Nikudel, M.R., 2016. Effect of injected bacterial suspension volume and relative density on carbonate precipitation resulting from microbial treatment. Ecol. Eng. 89, 49–55. https://doi.org/10.1016/J.ECOLENG.2016.01.010.

Salifu, E., MacLachlan, E., Iyer, K.R., Knapp, C.W., Tarantino, A., 2016. Application of microbially induced calcite precipitation in erosion mitigation and stabilisation of sandy soil foreshore slopes: a preliminary investigation. Eng. Geol. 201, 96–105. https://doi.org/10.1016/J.ENGGEO.2015.12.027.

Sang, G., Lunn, R.J., El Mountassir, G., Minto, J.M., 2023. Transport and fate of ureolytic *Sporosarcina pasteurii* in saturated sand columns: experiments and modelling. Transp. Porous Media 149, 599–624. https://doi.org/10.1007/s11242-023-01973-x.

Sharma, M., Satyam, N., Reddy, K.R., 2022. Large-scale spatial characterization and liquefaction resistance of sand by hybrid bacteria induced biocementation. Eng. Geol. 302, 106635 https://doi.org/10.1016/j.enggeo.2022.106635.

Skempton, A.W., 1954. The pore-pressure coefficients A and B. Geotechnique 4, 143–147. https://doi.org/10.1680/GEOT.1954.4.4.143.

Stocks-Fischer, S., Galinat, J.K., Bang, S.S., 1999. Microbiological precipitation of CaCO3. Soil Biol. Biochem. 31, 1563–1571. https://doi.org/10.1016/S0038-0717(99)00082-6.

Tagliaferri, F., Waller, J., Andò, E., Hall, S.A., Viggiani, G., Bésuelle, P., DeJong, J.T., 2011. Observing strain localisation processes in bio-cemented sand using x-ray imaging. Granul. Matter 133 (13), 247–250. https://doi.org/10.1007/S10035-011-0257-4, 2011.

Tan, Y., Gannon, J.T., Baveye, P., Alexander, M., 1994. Transport of bacteria in an aquifer sand: experiments and model simulations. Water Resour. Res. 30, 3243–3252. https://doi.org/10.1029/94WR02032.

Tang, C.S., Yin, L. Yang, Jiang, N. Jun, Zhu, C., Zeng, H., Li, H., Shi, B., 2020. Factors affecting the performance of microbial-induced carbonate precipitation (MICP) treated soil: a review. Environ. Earth Sci. 79, 1–23. https://doi.org/10.1007/S12665-020-8840-9/FIGURES/24.

Terzis, D., Laloui, L., 2018. 3-D micro-architecture and mechanical response of soil cemented via microbial-induced calcite precipitation. Sci. Rep. 81 (8), 1–11. https://doi.org/10.1038/s41598-018-19895-w, 2018.

Tobler, D.J., Cuthbert, M.O., Phoenix, V.R., 2014. Transport of *Sporosarcina pasteurii* in sandstone and its significance for subsurface engineering technologies. Appl. Geochem. 42, 38–44. https://doi.org/10.1016/j.apgeochem.2014.01.004.

Tobler, D.J., Minto, J.M., El Mountassir, G., Lunn, R.J., Phoenix, V.R., 2018. Microscale analysis of fractured rock sealed with microbially induced CaCO3 precipitation: influence on hydraulic and mechanical performance. Water Resour. Res. 54, 8295–8308.

van Paassen, L.A., 2011. Bio-mediated ground improvement: from laboratory experiment to pilot applications. In: Proceeding Geo-Frontiers; Adv. Geotech. Eng, pp. 4099–4108.

van Paassen, L.A., Ghose, R., van der Linden, T.J.M., van der Star, W.R.L., van Loosdrecht, M.C.M., 2010. Quantifying biomediated ground improvement by ureolysis: large-scale biogrout experiment. J. Geotech. Geoenviron. Eng. 136, 1721–1728. https://doi.org/10.1061/(ASCE)GT.1943-5606.0000382.

Verwey, E.J.W., Overbeek, J.T.G., 1955. Theory of the stability of lyophobic colloids. J. Colloid Sci. 10, 224–225.

Whiffin, V.S., 2004. Microbial CaCO3 Precipitation for the Production of Biocement. PhD Thesis. Murdoch University, Western Australia.

Whiffin, V.S., van Paassen, L.A., Harkes, M.P., 2007. Microbial carbonate precipitation as a soil improvement technique. Geomicrobiol J. 24, 417–423. https://doi.org/10.1080/01490450701436505.

Wu, S., Li, B., Chu, J., 2020. Large-scale model tests of biogrouting for sand and rock. Proc. Inst. Civ. Eng.: Ground Improv. https://doi.org/10.1680/JGRIM.18.00074.

Wu, S., Li, B., Chu, J., 2021. Stress-dilatancy behavior of MICP-treated sand. Int. J. Geomech. 21, 04020264. https://doi.org/10.1061/(ASCE)GM.1943-5622.0001923.

Wu, H., Wu, W., Liang, W., Dai, F., Liu, H., Xiao, Y., 2023. 3D DEM modeling of biocemented sand with fines as cementing agents. Int. J. Numer. Anal. Methods Geomech. 47, 212–240. https://doi.org/10.1002/NAG.3466.

Xiao, Y., Stuedlein, A.W., Ran, J., Evans, T.M., Cheng, L., Liu, H., van Paassen, L.A., Chu, J., 2019a. Effect of particle shape on strength and stiffness of biocemented glass beads. J. Geotech. Geoenviron. Eng. 145, 06019016. https://doi.org/10.1061/(ASCE)GT.1943-5606.0002165.

Xiao, Y., Yuan, Z., Lin, J., Ran, J., Dai, B., Chu, J., Liu, H., 2019b. Effect of particle shape of glass beads on the strength and deformation of cemented sands. Acta Geotech. 14, 2123–2131. https://doi.org/10.1007/S11440-019-00830-W/FIGURES/8.

Xiao, Y., Zhao, C., Sun, Y., Wang, S., Wu, H., Chen, H., Liu, H., 2021. Compression behavior of MICP-treated sand with various gradations. Acta Geotech. 16, 1391–1400. https://doi.org/10.1007/S11440-020-01116-2/FIGURES/7.

Xiao, Y., Ma, G., Wu, H., Lu, H., Zaman, M., 2022. Rainfall-induced erosion of biocemented graded slopes. Int. J. Geomech. 22, 04021256. https://doi.org/10.1061/(ASCE)GM.1943-5622.0002239/ASSET/ABF6AD87-28CC-4891-925A-5BA7A08E27D7/ASSETS/IMAGES/LARGE/FIGURE9.JPG.

Xu, S., Gao, B., Saiers, J.E., 2006. Straining of colloidal particles in saturated porous media. Water Resour. Res. 42, 12–16. https://doi.org/10.1029/2006WR004948.

Zamani, A., Montoya, B.M., 2019. Undrained cyclic response of silty sands improved by microbial induced calcium carbonate precipitation. Soil Dyn. Earthq. Eng. 120, 436–448. https://doi.org/10.1016/J.SOILDYN.2019.01.010.

Zeng, C., Veenis, Y., Hall, C.A., Young, E.S., van der Star, W.R.L., Zheng, J., van Paassen, L.A., 2021a. Experimental and numerical analysis of a field trial application of microbially induced calcite precipitation for ground stabilization. J. Geotech. Geoenviron. Eng. 147, 05021003. https://doi.org/10.1061/(ASCE)GT.1943-5606.0002545.

Zeng, H., Yin, L.Y., Tang, C.S., Zhu, C., Cheng, Q., Li, H., Lv, C., Shi, B., 2021b. Tensile behavior of bio-cemented, fiber-reinforced calcareous sand from coastal zone. Eng. Geol. 294, 106390 https://doi.org/10.1016/J.ENGGEO.2021.106390.